### POLITECNICO DI TORINO

Master's Degree in Communications Engineering



Master's Degree Thesis

# Radio Resource Management techniques with Multi-User MIMO for VLEO-NTN Systems

Supervisors

Prof. Roberto GARELLO

Dr. Daniel Gaetano RIVIELLO

Candidate

Bjorna ANAMALI

October 2025

#### Abstract

Non-Terrestrial Networks have gained increasing attention in the evolution of 5G and future 6G systems due to their ability to provide global connectivity, especially in under-served or hard-to-reach areas. In this context, Very Low Earth Orbit (VLEO) satellite constellations that operate at altitudes of 300-500 kilometers, are of specific interest as a result of decreased propagation delay and increased link budgets. On the other hand, such advantages come with challenges, as the high speed of VLEO satellites means strong Doppler shifts and rapidly varying link conditions. This calls for effective design of Radio Resource Management (RRM) schemes, which are critical to ensure proper service to the users.

This thesis investigates user scheduling strategies for NTNs, focusing on both location-based and Channel State Information (CSI)-based algorithms. Modifications to existing schemes are introduced to improve fairness and guarantee that all users are effectively scheduled. The user scheduling algorithms considered in this thesis are 4: Multiple Antenna Downlink Orthogonal clustering (MADOC), Distance-based MADOC (D-MADOC), Distance-based Minimum Clique Covering with DSatur (D-MCC-DSatur) and Heuristic-RRM (H-RRM), which are initially evaluated under a first scenario with uniformly distributed users. Simulation results show that, while MADOC and its distance based version, D-MADOC, achieve the highest peak sum-rate capacity, this is not exploited in all clusters. Instead, H-RRM and D-MCC-DSatur produce narrower cluster size distributions, leading to better exploitation of the resources.

Furthermore, the influence of varying satellite transmit power, expressed in terms of Equivalent Isotropically Radiated Power (EIRP), is analyzed. Performance is assessed using key performance indicators (KPIs) such as the cluster size, Signalto-Noise Ratio, throughput and outage. The results show that while CSI-based methods like MADOC and D-MADOC reach the highest peak capacities, their uneven clustering restricts fairness, particularly in low power conditions. In contrast, D-MCC-DSatur deliver a more even performance, resulting in lower outage levels and steadier throughput distributions for users. LB-SLNR beamforming consistently outperforms simple beam-steering, especially in environments with interference. This highlights the need for better precoding in 6G NTNs.

The study then extends to a more realistic dense-urban setting, where users are concentrated in populated areas, to capture the impact of non-uniform deployments. With users now closer to each other, it is more challenging for the beamformer to spatially separate them, leading to a reduced algorithm performance.

Additionally, early evaluations in a multi-satellite VLEO scenario indicate that user visibility of multiple satellites can improve coverage. An initial coverage and

visibility analysis was carried out for a VLEO constellation, looking at the spatial overlap between satellite footprints and user-satellite association. This preliminary study established the foundation for future evaluations of cooperative transmission and resource management across multiple satellites.

Overall, this thesis shows that designing adaptive, fairness-focused scheduling combined with better beamforming will be crucial for maximizing the potential of future broadband VLEO satellite networks.

# Acknowledgements

This work is not only the result of dedication and hard work, but also a reflection of the constant support of the people who believed in me when I doubted myself.

I would like to express my sincere gratitude to my supervisor, Professor Roberto Garello, for his true mentorship and constant support throughout this work. I am also deeply thankful to Daniel for his insightful ideas and willingness to explore new approaches, and to Gabriel for his helpful advice and thoughtful suggestions.

I am immensely grateful to my family for their constant support, encouragement, and belief in me throughout this journey. To my mother, father and my little brother, you never once questioned if I could make it. Your love and support have been my foundation and today I am happy to acknowledge that this achievement is as much yours as it is mine.

Finally, I would like to thank my friends. You gave me a reminder that home isn't always a place. Sometimes it's the people who sit right next to you, when everything familiar seems far away.

# Table of Contents

Li	st of	Tables	VII
Li	st of	Figures	VIII
A	crony	vms	XI
1	Intr	roduction	1
	1.1	Contributions	. 2
2	Sate	ellite Communication Systems	4
	2.1	NTN Platform Categories	. 5
		2.1.1 Airborne Platforms	. 7
		2.1.2 Comparative Perspective	. 7
	2.2	SatCom System Architecture	. 7
		2.2.1 Space Segment	. 8
		2.2.2 Ground Segment	. 9
		2.2.3 Communication Links	. 9
	2.3	NTN in 3GPP Standardization	. 10
3	Syst	tem Model	12
	3.1	System Description	. 12
	3.2	Antenna and Channel model	
	3.3	User Distribution	. 18
		3.3.1 Uniform user distribution	. 19
		3.3.2 Gaussian user distribution	. 21
	3.4	Beamforming	. 22
		3.4.1 Location-based Signal-to-Leakage-plus-Noise Ratio	
		3.4.2 Plain Beam-Steering	
4	Use	r Scheduling Algorithms	26
	4.1	MADOC	. 28

	4.2	D-MADOC	28
	4.3	D-MCC-DSatur	30
	4.4	Heuristic-RRM	31
5	Res	ults and performance evaluation	36
	5.1	Impact of Uniform User Distribution on Algorithm Performance	37
		$5.1.1$ Performance evaluation with EIRP equal to $30~\mathrm{dBW/MHz}$ .	38
		5.1.2 Performance evaluation with reduced EIRP	41
	5.2	Performance Evaluation under Hybrid User Distribution	48
		5.2.1 Sub-urban scenario	51
		5.2.2 Dense urban scenario	54
		5.2.3 Adaptive scenario	55
6	Cor	iclusion and Future Work	60
	6.1	Multi-Satellite Scenario	60
	6.2	Conclusion	65
$\mathbf{B}^{\mathbf{i}}$	ibliog	graphy	67

# List of Tables

3.1	Adopted terminology and notation	15
3.2	LOS Probability for Dense-Urban and Suburban Scenarios (Taken	
	from [37])	17
3.3	Shadow Fading Standard Deviation and Clutter Loss for Dense	
	Urban Scenario (Ka-band only, from [37])	18
3.4	Shadow Fading Standard Deviation and Clutter Loss for Subur-	
	ban/Rural Scenario (Ka-band only, from [37])	18
5.1	Simulation Parameters	38
5.2	Optimal thresholds for each algorithm	39
5.3	Mean cluster sizes (users/cluster)	40
5.4	Average metrics of the algorithms at EIRP = $30 \text{ dBW/MHz}$	41
5.5	Updated Simulation Parameters	42
5.6	Updated optimal thresholds for each algorithm	44
5.7	Optimal number of clusters for each algorithm	44
5.8	Summary of Adaptive Scenario Results for Different EIRP Values .	57

# List of Figures

2.1	Examples of satellite node topologies: a) star topology and b) mesh	_
2.2	topology [11]	5
2.2	NTN Platform categories [12]	6
2.3	Architecture of SatCom systems [18]	8
2.4	Classification of satellite coverage [20]	9
3.1	NTN System Architecture	13
3.2	Antenna Model Geometry from ITU-R M.2101-0 [34]	14
3.3	Earth-satellite geometry	19
3.4	Spherical coordinate system [41]	20
3.5	Uniform user distribution	21
3.6	Hybrid user distribution	22
4.1 4.2	Time and Space Division for Multi-User Access in NTN Discretized time allocation for cluster $p$ within the scheduling frame	27
	$T_{sch}$	27
5.1	Histogram of cluster size distribution for each algorithm	39
5.2	Sum-Rate Capacity CDF Comparison Across Algorithms	40
5.3	SINR CDF Comparison Across Algorithms	41
5.4	Throughput CDF Comparison Across Algorithms	42
5.5	Updated SINR CDF Comparison Across Algorithms	43
5.6	3D Plot of Throughput and Outage for MADOC	45
5.7	3D Plot of Throughput and Outage for D-MADOC	46
5.8	3D Plot of Throughput and Outage for D-Satur	47
5.9	Optimal Threshold selection and corresponding outage	48
5.10	Updated histogram of cluster size distribution for each algorithm	49
5.11	Updated Sum-Rate Capacity CDF Comparison Across Algorithms.	50
5.12	Updated Throughput CDF Comparison Across Algorithms	50
5.13	Optimal number of groups vs. Throughput and Outage	51
5.14	Histograms of users/cluster	52

5.15	Cumulative Distribution Function of SINR	52
5.16	Cumulative Distribution Function of Sum-Rate Capacity	53
5.17	Cumulative Distribution Function of Throughput	53
5.18	Optimal number of groups vs. Throughput and Outage	55
5.19	Histograms of users/cluster	55
5.20	Cumulative Distribution Function of SINR	56
5.21	Cumulative Distribution Function of Sum-Rate Capacity	56
5.22	Cumulative Distribution Function of Throughput	57
5.23	Adaptive Scenario: Threshold vs Throughput and Outage (EIRP=20	
	dbW/MHz)	58
5.24	Adaptive Scenario: Threshold vs Throughput and Outage (EIRP=30	
	dbW/MHz)	58
5.25	Adaptive Scenario: Threshold vs Throughput and Outage (EIRP=40	
	dbW/MHz)	59
6.1	VLEO Constellation for Multi-Sat scenario	62
6.2	Satellites considered for the coverage of Germany	62
6.3	Rectangle uniform user distribution for Multi-Sat scenario	63
6.4	User distribution and the satellites visible to each user	64

# Acronyms

**3GPP** 3rd Generation Partnership Project

**5G** Fifth Generation

**6G** Sixth Generation

**B5G** Beyond 5G

**BF** Beamforming

**CBF** Conventional Beamforming

**CCI** Co-Channel Interference

**CDF** Cumulative Distribution Function

CF Cell-Free

CL Clutter Loss

CSI Channel State Information

EIRP Equivalent Isotropically Radiated Power

eMBB enhanced Mobile Broadband

eMTC enhanced Machine Type Communications

FFR Full Frequency Reuse

FoV Field of View

**GEO** Geostationary Earth Orbit

**GSO** Geosynchronous Orbiting

**GW** Gateway

**HAPS** High Altitude Platform Systems

H-RRM Heuristic Radio Resource Management

**IoT** Internet of Things

**KPIs** Key Performance Indicators

LAPs Low Altitude Platforms

LB Location-based

**LEO** Low Earth Orbit

LOS Line of Sight

MEO Medium Earth Orbit

MIMO Multiple-Input Multiple-Output

MMSE Minimum Mean Square Error

MU Multi-User

NGSO Non-Geosynchronous Orbiting

**NLOS** Non-Line of Sight

 ${f NTN}$  Non-Terrestrial Network

PAC Per-Antenna Power Constraint

RRM Radio Resource Management

SINR Signal-to-Interference-plus-Noise Ratio

**SIR** Signal-to-Interference Ratio

SLNR Signal-to-Leakage-plus-Noise Ratio

SNR Signal-to-Noise Ratio

SPC Sum Power Constraint

SSP Sub-Satellite Point

SV Steering Vector

 ${\bf SDMA}$  Spatial Division Multiple Access

 $\mathbf{TDMA}$  Time Division Multiple Access

 ${f UAS}$  Unmanned Aerial System

**UAV** Unmanned Aerial Vehicle

**ULA** Uniform Linear Array

**UPA** Uniform Planar Array

 ${f UT}$  User Terminal

**VLEO** Very Low Earth Orbit

# Chapter 1

## Introduction

Non-Terrestrial Networks have gained increasing attention in the evolution of 5G and future 6G systems due to their ability to provide global connectivity, especially in under-served or hard-to-reach areas, where Terrestrial Networks (TNs) suffer to deliver service due to disruption or reduced capabilities [1].

The 5G Non-Terrestrial-Networks (NTNs) study began under 3GPP Release 17 and later continued under Release 21 that is anticipated to further expand NTN capability and lay an groundwork for 6G standardization [2]. Among all NTN architectures, Very Low Earth Orbit (VLEO) satellite constellations functioning at about 300–500 km altitudes have drawn particular interest. They have been appealing due to lower-propagation delays and favorable link budgets. These arrive, however, with some negative consequences: high orbital velocity of VLEO satellites results in strong Doppler effects and fast-varying link situations [2]. This is why efficient Radio Resource Management (RRM) mechanisms are needed to guarantee strong service provisioning.

Meeting traffic requirements of next B5G/6G networks is made even harder by scarcity of available spectra. To cope up, techniques on the efficient use of the spectrum have been studied, like Full Frequency Reuse (FFR) [3]. But FFR generates severe co-channel interference (CCI) that necessitates sophisticated methods of interference mitigation in transmitter's side, like Beamforming (BF), Multi-User MIMO (MU-MIMO), and optimized RRM schemes [3, 4, 5].

In real systems, the number of user terminals (UTs) is typically larger than the available transmit onboard satellite antennas. As a result, scheduling is an important part of system design. In this work, scheduling all users in the satellite coverage area is of primary objective. The users are collected in clusters and served through Spatial Division Multiple Access (SDMA) by means of digital beamforming (MU-MIMO) and clusters are time-multiplexed by TDMA. Finding an optimal grouping of users is an NP-complete problem, hence an excessive search is computationally expensive and heuristic methods are used instead [5].

The literature in [6] explored user scheduling techniques of downlink MU-MIMO systems and put forward hybrid greedy methods that offer capacity improvement along with user fairness. Following this thread of work, authors in [7] presented Multiple-Antenna Downlink Orthogonal Clustering (MADOC) that achieves low complexity clustering efficiently. Subsequently, [8] suggested a location-based version of it named Distance-based MADOC (D-MADOC) that exploits inter-user distance as a grouping metric rather than exploiting correlation coefficients. On a different trajectory of work, authors of [9, 10] came up with optimization-based methods such as a Mixed Integer Quadratic Programming model and a heuristic Radio Resource Management (H-RRM) algorithm aiming to minimize overall co-channel interference .

This thesis investigates user scheduling strategies for NTNs, focusing on both location-based and Channel State Information (CSI)-based algorithms. Modifications to existing schemes are introduced to improve fairness and guarantee that all users are effectively scheduled. The algorithms are first evaluated under a baseline scenario with uniformly distributed users. Simulation results show that, while D-MADOC achieves the highest peak sum-rate capacity, this is not exploited in all clusters. Instead, Heuristic RRM (H-RRM) and Distance-based Minimum Clique Covering with DSatur (D-MCC-DSatur) produce narrower cluster size distributions, leading to better exploitation of the resources. The study then extends to a more realistic dense-urban setting, where users are concentrated in populated areas, to capture the impact of non-uniform deployments. With users now closer to each other, it is more challenging for the beamformer to spatially separate them, leading to a reduced algorithm performance. Furthermore, the influence of varying satellite transmit power, expressed in terms of Equivalent Isotropically Radiated Power (EIRP), is analyzed. Performance is assessed using key performance indicators (KPIs) such as the cluster size, Signal-to-Noise Ratio, throughput and outage.

In the final part of this thesis, a preliminary study on a multi-satellite scenario is presented, focusing on user visibility and coverage overlap to lay the groundwork for future cooperative transmission and scheduling analysis.

#### 1.1 Contributions

This thesis was developed as part of the European Space Agency (ESA), Handover, Data Routing and Radio Resource Management for Very Low Earth Orbit (VLEO) Broadband Constellations (HANDING-OVER) project. The main contributions of this thesis are:

• Proposed modifications to the already existing state-of-the-art algorithms, to achieve fixed cluster allocation of users in VLEO satellite systems.

- Compared performance of CSI-based and Location-based scheduling algorithms in fixed cluster allocation scenarios.
- Analyzed and benchmarked beamforming techniques in multi-user MIMO NTN settings, highlighting the performance differences.
- Investigated user-level performance metrics such as throughput distribution, outage probability, and SINR to quantify fairness and robustness of each scheduling strategy in both uniform and dense-urban user distributions.
- Examined the impact of varying Equivalent Isotropically Radiated Power (EIRP) levels on overall system performance, providing insights into power-limited NTN operations.
- Developed an initial coverage and visibility study for a multi-satellite VLEO constellation, analyzing user-satellite association and spatial overlap among satellite footprints as a foundation for future cooperative transmission and distributed MIMO research.

This thesis is structured as follows: Chapter 2 introduces the fundamentals of satellite communication systems, outlining the categories of Non-Terrestrial Network (NTN) platforms, the architecture of satellite communication (SatCom) systems, and the integration of NTN within 3GPP standardization. Chapter 3 establishes the overall system model, including the antenna and channel model, the user distribution scenarios (both uniform and hybrid), and the beamforming techniques adopted. Chapter 4 focuses on user scheduling algorithms, presenting the proposed modifications and explaining their operational mechanisms. Chapter 5 discusses the simulation results, analyzing system performance under different user distributions, propagation conditions, and Equivalent Isotropically Radiated Power (EIRP) configurations. Finally, Chapter 6 presents the initial study on the multisatellite scenario and concludes the thesis by summarizing the main findings and outlining potential directions for future research.

# Chapter 2

# Satellite Communication Systems

Satellite communications (SATCOM) systems enable long-range voice and data communication via satellites, serving critical roles in aviation, defense, maritime, and remote terrestrial applications. This chapter will outline the key features of SatCom systems.

NTN Nodes Topology Non Terrestrial Network (NTN) nodes can be classified according to their topology, the type of links employed, and the nature of the connectivity services they provide to ground stations. From a topological perspective, NTN architectures are usually divided into two direct categories, which define how inter-node communication is organized:

- Star Topology: In this configuration, the network is arranged in a star shaped structure where each node communicates exclusively with a central node, often referred to as the hub. Furthermore, interconnection between different star topologies is attainable through their respective hubs, giving rise to a multi-star topology.
- Mesh Topology: In this arrangement, the network consists of a set of nodes such as satellites, ground stations, or user terminals where each node can directly communicate with any other via NTN links. This structure ensures redundancy and enables multiple communication paths, thereby enhancing the general reliability of the network.

Figure 2.1 illustrates these two satellite node topologies, depicting (a) the star topology and (b) the mesh topology.

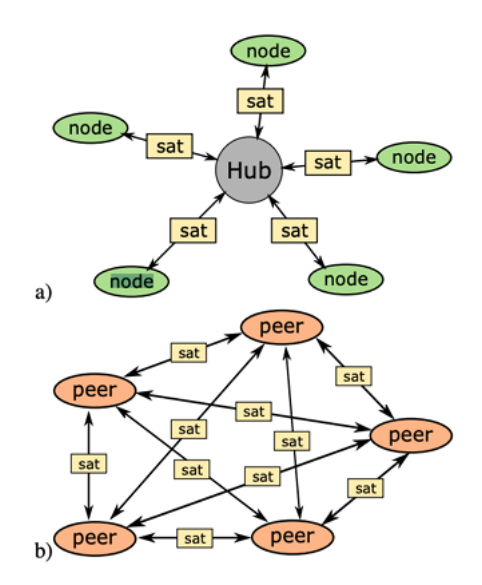


**Figure 2.1:** Examples of satellite node topologies: a) star topology and b) mesh topology [11].

#### 2.1 NTN Platform Categories

Non-Terrestrial Network (NTN) systems can be realized through a range of deployment platforms, which are broadly divided into *spaceborne* and *airborne* categories, as illustrated in Figure 2.2. This classification is generally determined by three factors: i) the *altitude*, or the platform's height above Earth's surface, ii) the *beam footprint size*, referring to the ground area covered by the transmitted beam, and iii) the *orbit*, which describes the regular, repeating trajectory of the platform in space.

**Spaceborne Platforms** The spaceborne segment of NTN is primarily composed of *Geosynchronous Orbiting (GSO)* and *Non-Geosynchronous Orbiting (NGSO)* satellites.

**GSO Satellites:** Operating at an altitude of 35,786 km, these satellites move synchronously with Earth's rotation. When their orbital plane lies on the equator, they achieve *Geostationary Earth Orbit (GEO)* status, appearing motionless in the sky to ground-based observers. GEO satellites typically provide beam footprints ranging from 200 km to 3,500 km [13, 14].

NGSO Satellites: Unlike GSO satellites, NGSO satellites do not remain fixed relative to Earth's surface. To ensure continuous coverage, they are deployed in constellations, with the number of satellites required increasing as orbital altitude

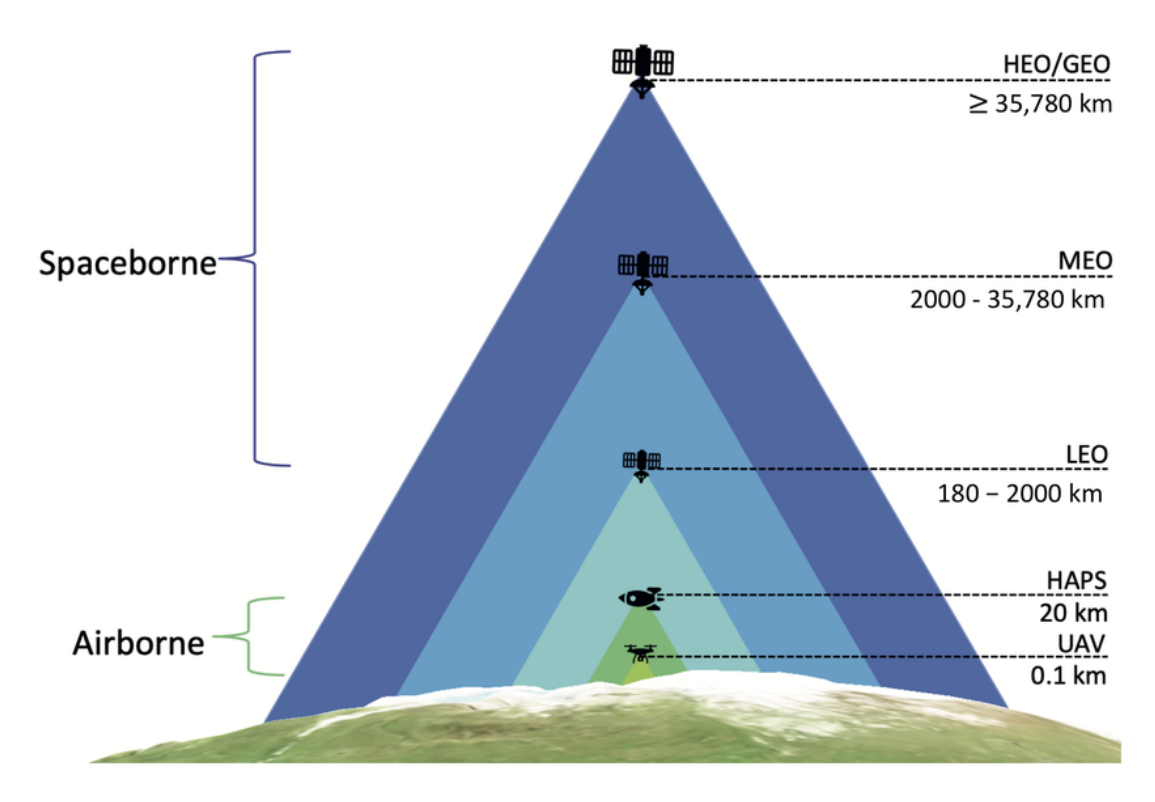


Figure 2.2: NTN Platform categories [12]

decreases. NGSO systems are typically classified into three categories:

- Low Earth Orbit (LEO): Positioned at altitudes of 300 km to 1,500 km, LEO satellites follow circular orbits and cover ground footprints of roughly 100 km to 1,000 km. Their balance of performance and scalability has made LEO the most widely adopted NGSO category.
- Medium Earth Orbit (MEO): Extending from 7,000 km to 25,000 km, MEO satellites usually employ circular orbits, though elliptical configurations are also used. Their footprints range from 100 km to 1,000 km.
- Very Low Earth Orbit (VLEO): Operating below 300 km, VLEO satellites are the most recent addition to NTN research. Their proximity to Earth enables extremely low latency and stronger link budgets compared to higher orbits. However, they face challenges such as atmospheric drag, higher fuel consumption for station-keeping, and shorter operational lifetimes.

#### 2.1.1 Airborne Platforms

Airborne NTN platforms operate closer to Earth's surface and are generally divided into *High-Altitude Platform Systems (HAPS)* and *Low-Altitude Platforms (LAPs)*.

**HAPS:** Deployed in the stratosphere at altitudes of 20 km to 50 km, HAPS act as aerial base stations providing localized coverage. They are especially valuable in regions where terrestrial infrastructure is impractical, such as remote or disaster-stricken areas. With their extended operational lifetimes and flexible positioning, HAPS provide an efficient solution for bridging connectivity gaps.

**LAPs:** Typically represented by *Unmanned Aerial Vehicles (UAVs)* operating at 100 m to 10,000 m. UAVs are expected to play a key role in future wireless networks by enabling rapid deployment, reliable Line-of-Sight (LoS) communication, and flexible mobility for coverage and capacity enhancement [15, 16]. However, widespread deployment faces challenges such as regulatory restrictions, costs, and public acceptance [17].

#### 2.1.2 Comparative Perspective

Among satellite platforms, **VLEO** and **LEO** systems offer the most attractive performance for emerging NTN applications. Their proximity to Earth significantly reduces propagation delays and improves link budgets compared to GEO and MEO satellites, leading to lower latency and higher achievable data rates. VLEO, in particular, provides unmatched latency but at the expense of increased operational complexity and shorter lifetimes.

Compared to airborne platforms such as HAPS and LAPs, **LEO and VLEO constellations** provide broader coverage and the capacity to simultaneously serve much larger populations. For these reasons, LEO satellites dominate current NTN deployments, while VLEO systems are gaining growing interest as a potential next step in NTN evolution.

#### 2.2 SatCom System Architecture

A Satellite Communication (SatCom) system, shown in Figure 2.3, is generally composed of three core components: the *space* segment, the *ground* segment, and the *communication links* that connect them. Together, these elements enable the provision of global services ranging from broadcasting and data delivery to broadband access and mobility support.

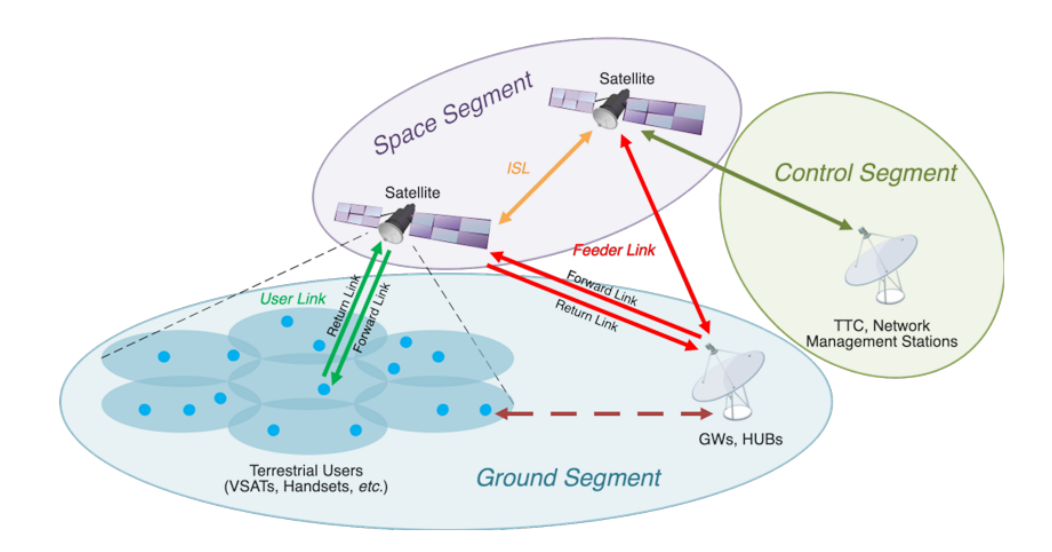


Figure 2.3: Architecture of SatCom systems [18]

#### 2.2.1 Space Segment

The space segment consists of active and spare satellites organized in constellations. Each satellite includes two main elements: the *payload*, which enables communication services, and the *platform*, which supports payload operation.

The payload typically comprises antennas and signal-processing equipment. Two main payload types exist:

Transparent payloads act as relays, amplifying and shifting the frequency of received signals before retransmission. Bandwidth is divided into sub-bands using input multiplexers (IMUX), amplified by transponders, and recombined using output multiplexers (OMUX). They are relatively simple in design but can also support beam routing and transponder hopping [19].

Regenerative payloads provide on-board processing capabilities such as modulation, coding, filtering, and routing. These payloads regenerate signals before retransmission, improving performance and enabling tighter integration with 5G/6G systems. However, they introduce challenges in terms of interoperability and standardization [19].

Satellites may generate either **single-beam** or **multi-beam** coverage (Fig. 2.4) [20]. Single-beam systems are simpler and serve focused regions, whereas multi-beam satellites can simultaneously cover multiple areas, increasing spectral efficiency and flexibility. Two beam strategies are widely used: **Earth-fixed beams**, which remain locked to a ground area within the field of view, and **Earth-moving beams**, which track the satellite's sub-satellite point (SSP) as it moves along its orbit [21].

Finally, the *platform* comprises supporting subsystems such as fuel for orbit

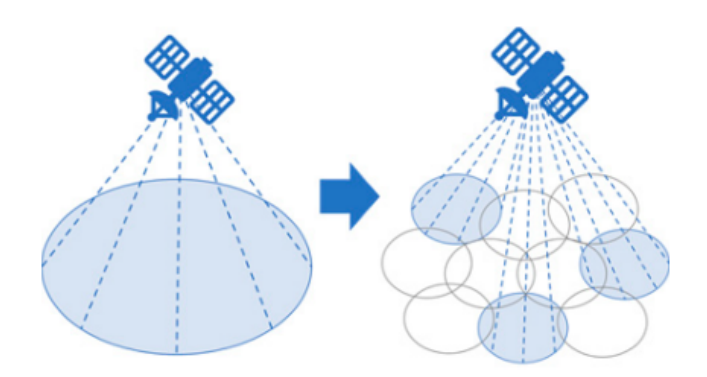


Figure 2.4: Classification of satellite coverage [20].

control, solar panels for power, and thermal and mechanical systems required to sustain payload operations.

#### 2.2.2 Ground Segment

The ground segment manages the space segment, ensures routing, and provides service delivery to end users. It consists of:

- User Terminals (UTs/UEs): End-user devices such as handheld terminals and Very Small Aperture Terminals (VSATs).
- Gateways (GWs): Interfaces between the satellite system and terrestrial networks. Future NTN architectures may allow direct device-to-device communication through satellites without gateway involvement.
- Service Stations: Hub or feeder stations aggregating and distributing data between user terminals and the space segment.
- Control Segment (TTC): Tracking, Telemetry, and Command stations that monitor satellites, send commands, and collect telemetry.

#### 2.2.3 Communication Links

Communication links connect the ground and space segments, as well as satellites to one another (Fig. 2.3). They are generally classified as [11]:

- 1. **Feeder Links:** Connect ground gateways to satellites, including uplinks and downlinks.
- 2. User Links: Connect satellites to user terminals, enabling end-user access.

3. Inter-Satellite Links (ISLs): Provide connectivity among satellites, supporting synchronization and data exchange. ISLs may be intra-orbital (e.g., LEO-LEO) or inter-orbital (e.g., GEO-LEO) and can operate using either radio-frequency or optical technologies.

Links can be further distinguished as **forward** (gateway-to-user) or **return** (user-to-gateway), and as **unidirectional** or **bidirectional**. While unidirectional links are common for broadcast services, bidirectional links are essential for interactive telecommunications. Depending on the service, connections may be point-to-point (unicast), point-to-multipoint (broadcast/multicast), multipoint-to-point (concentration), or multipoint-to-multipoint (mesh).

#### 2.3 NTN in 3GPP Standardization

The 3rd Generation Partnership Project (3GPP) is responsible for developing global mobile communication standards, which are published incrementally as Releases. Each release introduces new features and refinements after extensive technical discussions. The work of 3GPP is organized across three Technical Specification Groups (TSGs). The Radio Access Networks (RAN) group focuses on radio performance and protocol design; the Services and Systems Aspects (SA) group defines the overall architecture and service capabilities; and the Core Network and Terminals (CT) group specifies terminal interfaces, core network protocols, and interworking with external systems [22].

The integration of non-terrestrial networks (NTN) into 3GPP specifications began in March 2017, when initial study items were launched to assess NTN's potential role in 5G. Early investigations in Releases 15 and 16, notably documented in TR 38.811 and TR 38.821, examined NTN architectures, technical challenges, and candidate solutions across multiple layers. These studies addressed aspects of the physical layer, such as random access and timing advance, as well as protocollayer procedures, including HARQ and mobility management. They also considered architectural features such as tracking area management and network identities [23, 24].

A decisive milestone was reached with **Release 17**, completed in 2022, which introduced the first *normative* specifications for NTN integration into 5G. This release focused on minimizing changes to the user equipment (UE), the next-generation radio access network (NG-RAN), and the 5G Core (5GC), reusing terrestrial standards wherever possible. Two complementary access categories were defined. The first, NR-NTN, extends 5G New Radio to satellites in order to deliver enhanced Mobile Broadband (eMBB) services, especially for handheld devices. The second, IoT-NTN, enables NB-IoT and eMTC-based communications via satellite,

thereby addressing massive machine-type communication (mMTC) applications in domains such as agriculture, logistics, transport, and security [25, 26].

Building upon this foundation, **Release 18** further enhances NTN capabilities by supporting frequencies above 10 GHz, improving mobility and uplink coverage performance, and extending multicast and broadcast functions. This release also aims to align NR-NTN and IoT-NTN specifications more closely, ensuring seamless integration of both access modes within the broader 5G system. Looking forward, **Releases 19 and 20** are expected to expand NTN functionalities even further, introducing features such as regenerative payloads, multi-connectivity, downlink Peak-to-Average Power Ratio (PAPR) optimization, and enhanced mechanisms for capacity and coverage management [27, 28, 29, 30].

The evolution of NTN standardization highlights a broader paradigm shift in mobile communications. Prior to 5G, terrestrial (TN) and non-terrestrial (NTN) systems were studied separately, with little overlap in optimization. With 5G and 5G-Advanced, the objective has shifted toward their integration while limiting disruptions to existing terrestrial standards. In the 6G era, TN and NTN are expected to be jointly optimized within a unified multi-layered architecture, where satellite and terrestrial segments function as complementary components of a single infrastructure. This trend is reinforced by the growing alignment between 3GPP NTN specifications and the standardization work of the ITU-R, which increasingly incorporates NTN into the International Mobile Telecommunications (IMT) framework [31].

# Chapter 3

# System Model

#### 3.1 System Description

The Satellite Communication (SatCom) system architecture comprises a number of interconnected segments as shown in Figure 3.1, and the terrestrial or **ground segment** forms a core part of resource and network management functions. Specifically, the Gateway (GW) stations are the calculation centers responsible for determining the parameters for Radio Resource Management (RRM) such as scheduling and beamforming. When scheduling based on Channel State Information (CSI) is taken into account, the gNodeB (gNB) or GW transmit the pilot signals for the downlink directions towards the user terminals that can estimate the respective downlink CSI. The CSI estimates are then transmitted back to the gNB, which uses the estimates to execute optimal user scheduling choices. In the event of location-based schedulingthe gNB estimates the user positions and correspondingly calculates scheduling strategies based on just locational information and hence without CSI feedback. This dual approach to scheduling, using either channel information or user location, highlights how digital technologies can improve the efficiency and flexibility of communication systems.

Regarding the **on-board segment**, the simulation considers a single multibeam Very Low Earth Orbit (VLEO) satellite operating at an altitude of  $h_{\rm sat}=310$  km. The **user segment** is equipped with a VSAT-type receiver, where the antennas of the users are directly pointed to the satellite, compliant with specifications outlined in the 3GPP Technical Report 38.821 [32].

Regardless if we are considering CSI-based or location-based algorithms for the scheduling, there is a mismatch on the channel used for the computation of the beamforming coefficients and the actual channel used for transmission. This is due to the transmission between the UE and the GW, and then GW to the satellite. Referring back to Figure 3.1, the actual beamformed symbols are transmitted to

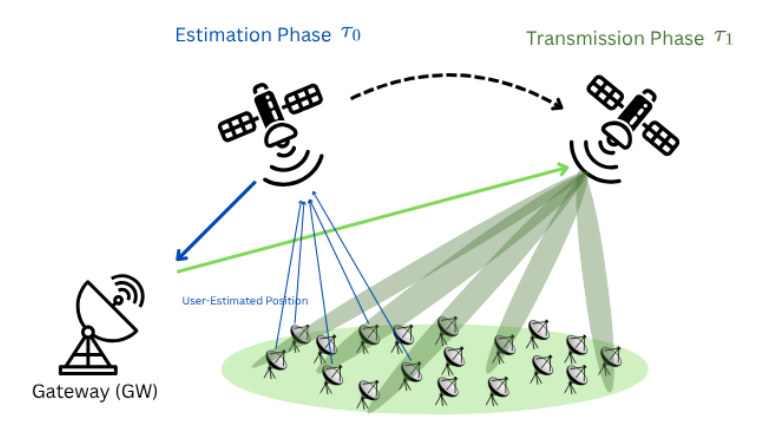


Figure 3.1: NTN System Architecture

the users at time instant  $\tau_1 = \tau_0 + \Delta \tau$ , where  $\Delta \tau$  is the latency between the channel estimation and transmission phases, causing a mismatch between the channel used for beamforming and scheduling at time  $\tau_0$ , and the actual channel used for transmission at time  $\tau_1$ . This latency  $\Delta \tau$  comprises the maximum propagation delay on the uplink user link within the coverage area  $\tau_{UE,\eta_{\text{max}}}$ , the downlink/uplink propagation delay  $\tau_{GW,\eta_{\text{max}}}$  to/from the GW, also assumed to be on the edge of the coverage area, processing delay  $\tau_p$  for RRM and additional system delay  $\tau_{Sys}$ :

$$\Delta \tau = \tau_{UE,\eta_{\text{max}}} + 2\tau_{GW,\eta_{\text{max}}} + \tau_{Sys} \tag{3.1}$$

**Notation:** Throughout this thesis, and if not otherwise specified, the following notation is used: **a** and **A** denote vectors and matrices, respectively.  $\mathbf{A}^{\mathrm{T}}$  and  $\mathbf{A}^{\mathrm{H}}$  denotes the transpose and the conjugate transpose of matrix **A**, respectively.  $[\mathbf{A}]_{i,j}$  denotes the element in the *i*-th row and the *j*-th column, while  $[\mathbf{A}]_{i,j}$  and  $[\mathbf{A}]_{:,j}$  denote the *i*-th row and the *j*-th column of matrix **A**, respectively.  $\mathrm{tr}(\mathbf{A})$  denotes the trace of matrix **A**, while  $\mathrm{diag}(a_1, \dots, a_K)$  denotes a diagonal matrix. Finally,  $\mathbf{0}_N$  and  $\mathbf{1}_N$  indicate a  $N \times 1$  vector of 0's and 1's, respectively, while  $\otimes$  indicates the Kronecker product.

#### 3.2 Antenna and Channel model

The single VLEO MU-MIMO satellite is equipped with an on-board Uniform Planar Array (UPA) which lies on the (y, z) plane, as shown in Figure 3.2. The UPA consists of  $N = N_y \times N_z$  elements, where  $N_y$  and  $N_z$  is the number of elements along

the y-axis and the z-axis, respectively. The antenna elements are characterized by the radiation pattern  $g_E(\vartheta_k, \varphi_k)$ , with parameters described in the 3GPP Technical Report 38.901 [33].

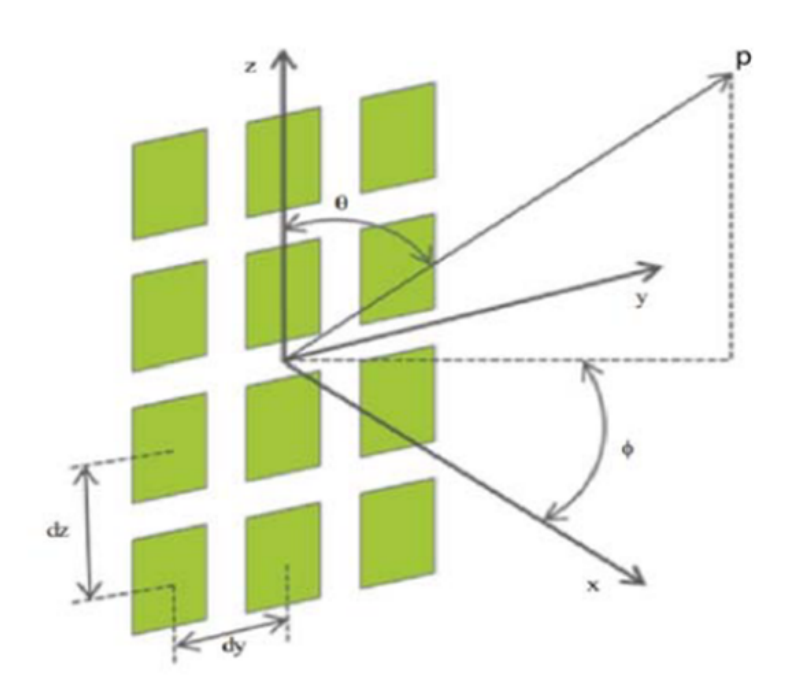


Figure 3.2: Antenna Model Geometry from ITU-R M.2101-0 [34]

The UPA array gain can be determined by taking the scalar product of the location matrix of the antenna elements  $\mathbf{P} \in \mathbb{R}^{3 \times N}$  and the spherical unit vector  $\mathbf{r}$  defined as

$$\mathbf{r} = [0, \sin \theta_k \sin \varphi_k, \cos \theta_k] \tag{3.2}$$

which corresponds to the direction of departure in terms of zenith angle  $\vartheta_k$  and azimuth angle  $\varphi_k$  for the k-th user [35, 36]:

$$\mathbf{a}_{UPA}(\vartheta_k, \varphi_k) = \exp\left(j\frac{2\pi}{\lambda}\mathbf{r_k}\,\mathbf{P}\right) \tag{3.3}$$

where  $\mathbf{P}$  contains in its rows the Cartesian coordinates of the antenna elements:

$$\mathbf{P} = \begin{bmatrix} \mathbf{0}_{N}, \ (\mathbf{1}_{N_{z}} \otimes \mathbf{d}_{y}), \ (\mathbf{d}_{z} \otimes \mathbf{1}_{N_{y}}) \end{bmatrix}^{\mathsf{T}}$$
(3.4)

And  $\mathbf{d}_y$  and  $\mathbf{d}_z$  give the antenna element positions along the y and z axes, respectively:

$$\mathbf{d}_{y} = d_{H} [0, 1, \dots, N_{y} - 1]^{\mathsf{T}}$$
(3.5)

$$\mathbf{d}_z = d_V [0, 1, \dots, N_z - 1]^{\mathsf{T}} \tag{3.6}$$

 Table 3.1: Adopted terminology and notation

Notation	Definition
k	Boltzmann constant
B	User bandwidth
$T_k$	Equivalent noise temperature of user $k$
$d_k$	Slant range of user terminal $k$
$\lambda$	Carrier wavelength
$G_k^{(\mathrm{rx})}$	Reception antenna gain for user $k$

Therefore, the entry of user-k's array gain for antenna element  $(n_y, n_z)$  can be written as

$$\left[\mathbf{a}_{\text{UPA}}(\vartheta_k, \varphi_k)\right]_n = \exp\left\{j\frac{2\pi}{\lambda} \left(d_{\text{H}} n_y \sin \vartheta_k \sin \varphi_k + d_{\text{V}} n_z \cos \vartheta_k\right)\right\}, \quad (3.7)$$

with the mapping between index n and the antenna coordinates  $(n_y, n_z)$  given by

$$n = (N_z - 1) n_z + n_y + 1, \quad n_y \in \{0, \dots, N_y - 1\}, \ n_z \in \{0, \dots, N_z - 1\}.$$
 (3.8)

Finally, the  $1 \times N$  steering vector (SV) of the UPA in the direction of the k-th UT can be expressed as:

$$\mathbf{a}(\vartheta_k, \varphi_k) = g_E(\vartheta_k, \varphi_k) \, \mathbf{a}_{UPA}(\vartheta_k, \varphi_k). \tag{3.9}$$

Next, we define the inferred channel matrix as:

$$\widehat{\mathbf{H}} = \left[ \widehat{\mathbf{h}}_{1}^{\mathsf{T}}, \widehat{\mathbf{h}}_{2}^{\mathsf{T}}, \dots, \widehat{\mathbf{h}}_{K}^{\mathsf{T}} \right]^{\mathsf{T}}$$
(3.10)

of size  $K \times N$ , where the k-th row corresponds to the channel vector associated with the k-th user. Similarly, the n-th column collects the channel coefficients from the n-th antenna feed to all K user terminals. More in depth, the k-th row of  $\widehat{\mathbf{H}}$  can be inferred from UT-k's position by computing the slant range  $d_k$  and the UT's direction  $(\vartheta_k, \varphi_k)$  with respect to the UPA:

$$\hat{\mathbf{h}}_k = G_k^{(\text{rx})} \frac{\lambda}{4\pi d_k} \sqrt{\frac{1}{kBT_k}} e^{-j\frac{2\pi}{\lambda}d_k} \mathbf{a}(\vartheta_k, \varphi_k)$$
(3.11)

An overview of the notation used for this equation follows in Table 3.1.

 $G_k^{(rx)}$  is the maximum reception gain of the k-th user terminal's antenna, which is assumed to be a VSAT based on the 3GPP model reported in [37], pointed towards the satellite [38].

It must be noted that, if we consider additional losses  $L_k$  experienced by the k-th UT due to shadowing, scintillation and atmospheric attenuation, the real channel vector can be written as  $\mathbf{h}_k = \sqrt{L_k} \, \hat{\mathbf{h}}_k$ , where  $L_k$  is given by contributions of log-normal shadowing  $(L_{sha,k})$ , atmospheric attenuation  $(L_{atm,k})$ , scintillation  $(L_{sci,k})$ , and finally, clutter loss  $(L_{cl,k})$ :

$$L_k = L_{sha,k} \cdot L_{atm,k} \cdot L_{sci,k} \cdot L_{cl,k} \tag{3.12}$$

Therefore, the actual Feed-Space (FS) channel vector  $\mathbf{h}_k$  encountered during propagation can be written as:

$$\mathbf{h}_{k} = G_{k}^{(\mathrm{rx})} \frac{\lambda}{4\pi d_{k}} \sqrt{\frac{L_{sha,k} \cdot L_{atm,k} \cdot L_{sci,k} \cdot L_{cl,k}}{kBT_{k}}} e^{-j\frac{2\pi}{\lambda}d_{k}} \mathbf{a}(\vartheta_{k}, \varphi_{k})$$
(3.13)

The statistics of  $L_k$  (3.12) depend on whether user k is in Line-of-Sight (LOS) or Non-Line-of-Sight (NLOS) conditions, according to a LOS probability that depends on its elevation angle [37].

To determine whether a UE experiences Line-of-Sight (LOS) or Non-Line-of-Sight (NLOS) conditions, the model first computes the elevation angle  $\epsilon$  which is the angle between the horizontal plane at the UE location and the line connecting the UE to the satellite. According to the Earth-satellite geometry depicted in Figure 3.3, the elevation angle is related to the Earth central angle  $\lambda$  and the nadir angle  $\eta$  by the equation:

$$\epsilon + \lambda + \eta = 90^{\circ} \tag{3.14}$$

If the nadir angle  $\eta$  and the satellite's Field of View (FoV)  $\eta_0$  are known, the elevation angle can be computed from:

$$\cos \epsilon = \frac{\sin \eta}{\sin \eta_0} \tag{3.15}$$

where  $\eta_0 = \arcsin\left(\frac{R_E}{R_E + h_{\text{sat}}}\right)$  is the satellite's Field of View (FoV),  $R_E$  is the Earth radius, and  $h_{\text{sat}}$  is the satellite altitude.

A higher elevation angle generally corresponds to a clearer path to the satellite, resulting in a higher probability of LOS. This relationship is modeled using empirical LOS probability curves specified by the 3GPP TR 38.811 standard, as summarized in Table 3.2. As the elevation angle increases, the Line-of-Sight (LOS) probability steadily rises in both dense-urban and suburban scenarios; however, suburban environments consistently exhibit significantly higher LOS probabilities, especially at lower elevation angles, due to fewer obstructions in the signal path.

Once the LOS/NLOS condition is determined probabilistically based on the elevation angle  $\epsilon$ , the path loss and shadow fading are modeled differently depending on that condition. Specifically, 3GPP defines separate statistical distributions for shadow fading in LOS and NLOS cases. For both conditions, log-normal shadowing is applied, but with different standard deviations:

**Table 3.2:** LOS Probability for Dense-Urban and Suburban Scenarios (Taken from [37])

Elevation Angle	Dense-Urban	Suburban
10°	28.2%	78.2%
20°	33.1%	86.9%
30°	39.8%	91.9%
40°	46.8%	92.9%
50°	53.7%	93.5%
60°	61.2%	94.0%
70°	73.8%	94.9%
80°	82.0%	95.2%
90°	98.1%	99.8%

- In LOS conditions, the shadow fading component  $L_{\text{sha},k}$  follows a log-normal distribution with a smaller standard deviation.
- In NLOS conditions, the variance is significantly higher to account for increased unpredictability due to obstructions.

The shadow fading loss is represented by a random variable F, generated from a normal distribution, i.e.,  $F \sim \mathcal{N}(0, \sigma_{SF}^2)$ , where  $\sigma_{SF}$  denotes the standard deviation of shadow fading in dB. The value of  $\sigma_{SF}$  depends on the user's environment (e.g., dense urban or suburban) and whether the propagation condition is LOS or NLOS.

According to 3GPP TR 38.811 [37], tables are provided for reference elevation angles from 10° to 90° at both S-band and Ka-band frequencies. For a UE at a given elevation angle  $\epsilon_k$ , the standard deviation  $\sigma_{\rm SF}$  and the clutter loss  $L_{{\rm cl},k}$  should be chosen by selecting the values from the table corresponding to the closest reference angle to  $\epsilon_k$ .

Moreover, in LOS conditions, the clutter loss is considered negligible and is typically set to 0 dB in the basic path loss model. In contrast, for NLOS cases, clutter loss is included explicitly as an additional attenuation term  $L_{cl,k}$ , also provided in the same tables.

Tables 3.3 and 3.4 list the shadow fading standard deviation and clutter loss for the dense urban and suburban/rural scenarios, respectively.

Additionally, atmospheric attenuation  $L_{\text{atm},k}$ , scintillation loss  $L_{\text{sci},k}$ , and clutter loss  $L_{\text{cl},k}$  are included as multiplicative loss components as per Equation 3.12. The terms  $L_{\text{atm},k}$  and  $L_{\text{sci},k}$  model additional losses encountered by the signal as it propagates through the atmosphere. Atmospheric attenuation  $L_{\text{atm},k}$  is computed according to ITU-R P.676 [39], and accounts for oxygen and water vapor absorption, which depend on frequency, humidity, and the slant path length determined by the

**Table 3.3:** Shadow Fading Standard Deviation and Clutter Loss for Dense Urban Scenario (Ka-band only, from [37])

Elevation	$\sigma_{\rm SF}^{ m LOS}$ / $\sigma_{\rm SF}^{ m NLOS}$ (dB)	$L_{\rm cl} \ ({ m dB})$
10°	2.9 / 17.1	44.3
20°	2.4 / 17.1	39.9
30°	2.7 / 15.6	37.5
40°	2.4 / 14.6	35.8
50°	2.4 / 14.2	34.6
60°	2.7 / 12.6	33.8
70°	2.6 / 12.1	33.3
80°	2.8 / 12.3	33.0
90°	0.6 / 12.3	32.9

**Table 3.4:** Shadow Fading Standard Deviation and Clutter Loss for Suburban/Rural Scenario (Ka-band only, from [37])

Elevation	$\sigma_{\rm SF}^{ m LOS}$ / $\sigma_{\rm SF}^{ m NLOS}$ (dB)	$L_{\rm cl} \ ({ m dB})$
10°	1.9 / 10.7	29.5
20°	1.6 / 10.0	24.6
30°	1.9 / 11.2	21.9
40°	2.3 / 11.6	20.0
50°	2.7 / 11.8	18.7
60°	3.1 / 10.8	17.8
70°	3.0 / 10.8	17.2
80°	3.6 / 10.8	16.9
90°	0.4 / 10.8	16.8

UE's elevation angle. Scintillation loss  $L_{\text{sci},k}$  represents rapid signal fluctuations due to atmospheric turbulence, modeled as log-normal fading based on ITU-R P.618 [40]. The severity of scintillation depends on the frequency band, elevation angle, and regional climate conditions.

#### 3.3 User Distribution

This thesis considers mainly two different user distributions to evaluate the performance of the scheduling and beamforming algorithms. Initially, a uniform user distribution is considered, in which users are uniformly distributed within the coverage area of the satellite. Additionally, this thesis presents results with some of the users concentrated in cities, to mirror a dense-urban scenario, probably more

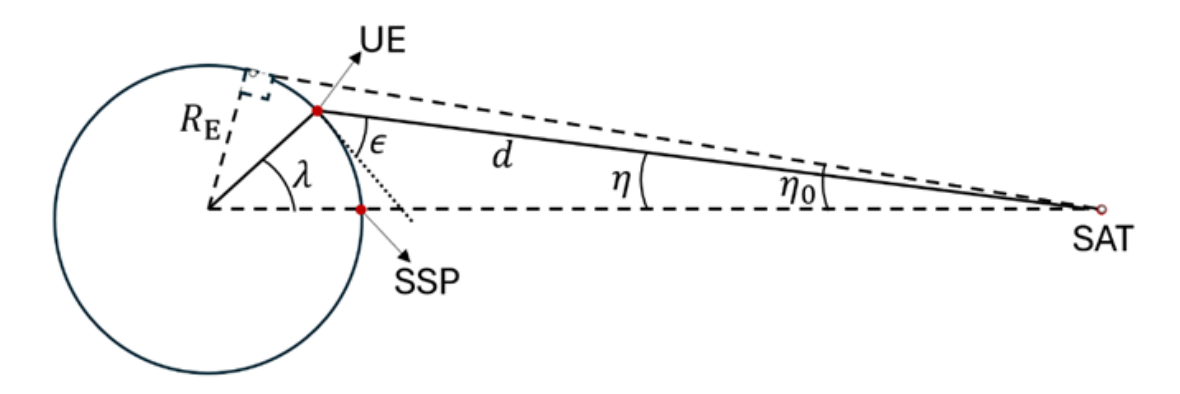


Figure 3.3: Earth-satellite geometry.

representative of the real-life scenarios.

#### 3.3.1 Uniform user distribution

Figure 3.3 shows the Earth-satellite geometry. Two angles play a crucial role on the definition of the size of the coverage area of the satellite, and therefore of the placement of the users. The off-nadir angle  $\eta$  is the angle between the satellite's nadir (or, SSP) and the edge of its field of view, measured from the satellite. The Earth-central angle  $\lambda$  is the angle at the Earth's center between the SSP and the edge of the footprint, measured from Earth's center.

For a specific UE,  $\eta$  is the off-nadir angle,  $\lambda$  is the Earth Central angle, while the distance between the user and the satellite, called slant range, is computed as:

$$d_k = R_E \frac{\sin(\lambda)}{\sin(\eta)} = (R_E + h_{sat}) \frac{\sin(\lambda)}{\cos(\epsilon_k)}$$
(3.16)

As seen before, the satellite's field of view (FoV) is denoted by  $\eta_0 = \arcsin \frac{R_E}{R_E + h_{sat}}$ . The satellite footprint, or the satellite coverage area is defined by a spherical cap limited by a maximum off-nadir angle  $\eta_{max} = 50^{\circ}$ , or a corresponding maximum Earth-central angle  $\lambda_{max}$ :

$$\lambda_{max} = 90^{\circ} - \eta_{max} - \cos^{-1} \left( \frac{\sin \eta_{max}}{\sin \eta_0} \right)$$

The maximum Earth-central angle  $\lambda_{max}$  defines the size of the footprint on the ground, or the boundary on the spherical cap where users can be placed.

The distribution of the users is defined by the user density  $\rho_{UEs}$ , which by definition is the number of users per km<sup>2</sup>. The K users are uniformly generated on a spherical cap initially centered at the North Pole, using a spatial Poisson process

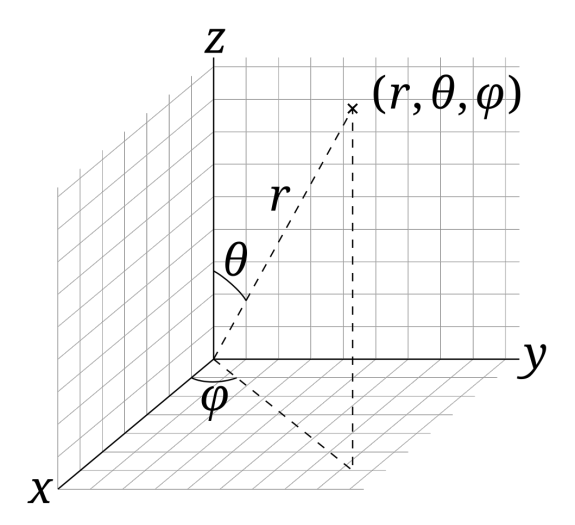


Figure 3.4: Spherical coordinate system [41]

defined by the user density  $\rho_{UEs}$ . The total number of users in the coverage area is then modeled as a Poisson random variable

$$K \sim \text{Poisson}(\rho_{UEs} |\mathcal{S}|)$$

where  $|\mathcal{S}| = 2\pi R_E^2 (1 - \cos \lambda_{max})$  is the coverage area, and  $R_E$  is the Earth's radius. Having obtained the number of users K corresponding to the user density  $\rho_{UEs}$ , the users are placed uniformly within the cap, using spherical coordinates using the convention in Figure 3.4. To achieve the uniform distribution, the azimuth angle  $\phi$  is sampled uniformly in  $[-\pi, \pi]$ , instead the polar angle  $\theta$  is generated according to:

$$\theta = \arccos(U(\cos(\lambda_{max}) - 1) + 1)$$
 where  $U \sim U(0,1)$ 

to ensure that  $\cos(\theta)$  is uniformly distributed in  $[\cos(\lambda_{max}),1]$  and therefore the user positions are uniform across the spherical cap.

After generating the user positions on the reference spherical cap centered at the North Pole, a transformation is needed to place them over the actual area covered by the satellite on Earth. This transformation aligns the users with the sub-satellite point (SSP), which is defined by the satellite's latitude  $\phi_{\text{SSP}}$  and longitude  $\lambda_{\text{SSP}}$ . To achieve this, active rotations in  $\mathbb{R}^3$  are applied to the users' Cartesian coordinates.

The transformation consists of two sequential rotations:

- 1. A rotation around the y-axis by an angle  $(90^{\circ} \phi_{\rm SSP})$ , which moves the spherical cap from the pole to the correct latitude;
- 2. A rotation around the z-axis by an angle  $\lambda_{\rm SSP}$ , which aligns the cap with the correct longitude.

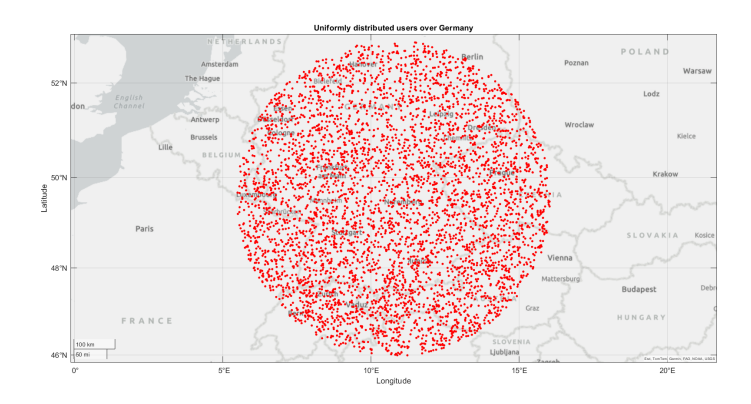


Figure 3.5: Uniform user distribution

The rotated user coordinates  $\mathbf{r}_{rot}$  can be expressed as:

$$\mathbf{r}_{\rm rot} = \mathbf{R}_z(\lambda_{\rm SSP}) \, \mathbf{R}_y(90^{\circ} - \phi_{\rm SSP}) \, \mathbf{r}_{\rm pole}$$

where  $\mathbf{r}_{\text{pole}}$  represents the initial user coordinates on the North Pole-centered cap, while  $\mathbf{R}_{y}(\cdot)$  and  $\mathbf{R}_{z}(\cdot)$  are the standard rotation matrices around the y and z axes [42], defined as:

$$\mathbf{R}_{y}(\theta) = \begin{bmatrix} \cos \theta & 0 & \sin \theta \\ 0 & 1 & 0 \\ -\sin \theta & 0 & \cos \theta \end{bmatrix}, \qquad \mathbf{R}_{z}(\theta) = \begin{bmatrix} \cos \theta & -\sin \theta & 0 \\ \sin \theta & \cos \theta & 0 \\ 0 & 0 & 1 \end{bmatrix}. \tag{3.17}$$

It is important to note that the order of these rotations matters, since rotation matrices do not commute. In this work, the chosen sequence (first y, then z) follows an **extrinsic** rotation convention, meaning the rotations are applied with respect to the fixed global coordinate system [42]. This approach ensures that the users' positions are correctly relocated from the reference cap to the actual satellite footprint, preserving their geographic orientation on the Earth's surface.

An example of this user distribution in 2D is shown in Figure 3.5.

#### 3.3.2 Gaussian user distribution

In real world scenarios, where users are mainly concentrated in inhabitated areas, the uniform distribution might not be the most representative one. Considering the large number of users around cities, it is possible to deploy a hybrid user distribution, where a large portion of the K users is centered around cities, and the remaining percentage is uniformly distributed within the coverage area. Each city center defines the mean  $(\mu_{lat}, \mu_{lon})$  of a Gaussian distribution, with a standard

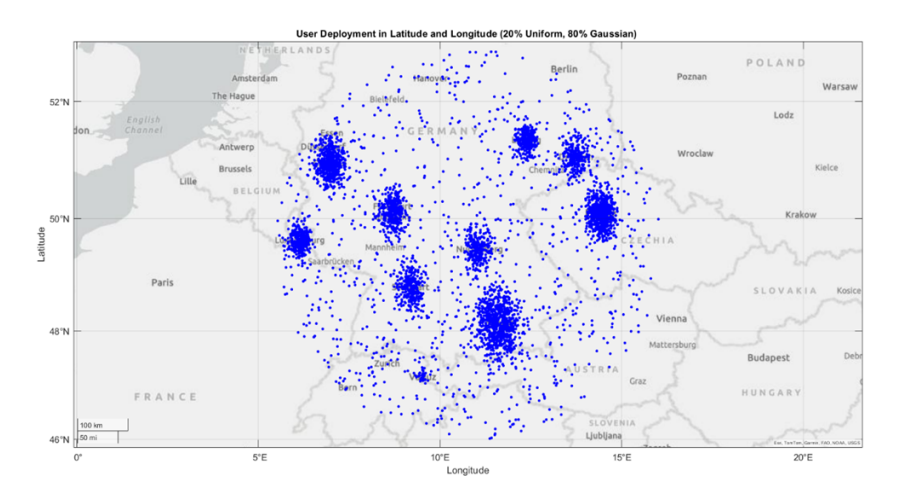


Figure 3.6: Hybrid user distribution

deviation  $\sigma$  proportional to the area of the city. The number of users associated to each city is proportional to its real population. Therefore, to mimic dense-urban hotspots, large cities are represented by more users and larger spreads. Chapter 5 presents results obtained under a hybrid UT distribution, where 80% of the users follow a Gaussian placement around cities and 20% are placed uniformly over the footprint.

A representation of this distribution scheme is shown in Figure 3.6.

#### 3.4 Beamforming

Beamforming is a spatial precoding technique that leverages antenna arrays to control the radiation pattern of transmitted signals. By assigning complex weights to individual antenna elements, the transmitter can create constructive interference at the intended receiver and destructive interference in other directions. This capability enhances spectral efficiency, minimizes interference, and improves overall system fairness.

In general, beamforming can be formulated as a linear precoding strategy. Let  $\mathbf{H} \in \mathbb{C}^{K \times N}$  represent the channel matrix between a transmitter equipped with N antennas and K users. The transmitted signal vector  $\mathbf{x}$  can be expressed as:

$$\mathbf{x} = \sum_{k=1}^{K} \mathbf{w}_k s_k, \tag{3.18}$$

where  $s_k$  denotes the data symbol intended for user k, and  $\mathbf{w}_k \in \mathbb{C}^{N \times 1}$  is the corresponding beamforming (precoding) vector used to spatially shape the signal. The received signal at user k is then given by:

$$y_k = \mathbf{h}_k^H \mathbf{w}_k s_k + \sum_{\substack{j=1\\j\neq k}}^K \mathbf{h}_k^H \mathbf{w}_j s_j + n_k$$
(3.19)

where  $\mathbf{h}_k \in \mathbb{C}^{N \times 1}$  represents the channel vector for user k, and  $n_k$  is additive white Gaussian noise. The first term corresponds to the desired signal component, while the second term accounts for inter-user interference.

The objective of beamforming is to optimize the beamforming vectors  $\{\mathbf{w}_k\}$  to maximize the strength of the desired signal while suppressing interference.

#### 3.4.1 Location-based Signal-to-Leakage-plus-Noise Ratio

In this thesis, the beamforming design follows a location-based Signal-to-Leakage-plus-Noise Ratio (LB-SLNR) formulation, also expressed as location-based Minimum Mean Square Error (LB-MMSE) through a proper normalization. The qualifier location-based suggests that user position information (latitude, longitude, elevation angle, and slant range) can be exploited to reconstruct the channel information instead of using pilots. As explained before, performing the process of channel estimation using downlink pilots would lead to huge overhead and latency associated with full CSI acquisition. Using the users' position leads to the construction of an inferred channel matrix  $\hat{\mathbf{H}}$ , with elements as defined in (3.11).

The beamforming procedure is outlined in the pseudocode of Algorithm 1, where the input is the inferred channel matrix  $\widehat{\mathbf{H}} \in \mathbb{C}^{N \times K}$ , with N the number of transmit antennas and K the number of users. For each cluster  $C_p$ , with size  $K_p$ , the corresponding sub-matrix  $\widehat{\mathbf{H}}_p$  is extracted. A regularization factor  $\alpha_p = K_p/P_t$  is introduced, which depends on the cluster size  $K_p$  and the available transmit power  $P_t$ .

The precoding matrix  $\mathbf{W}_p$  is then computed as:

$$\mathbf{W}_{p} = \widehat{\mathbf{H}}_{p}^{H} \left( \widehat{\mathbf{H}}_{p} \widehat{\mathbf{H}}_{p}^{H} + \alpha_{p} \mathbf{I}_{K_{p}} \right)^{-1}, \tag{3.20}$$

which corresponds to an MMSE-type solution where interference leakage and noise are jointly accounted for. Under the assumption of single-antenna users and Equal Power Allocation (EPA), where each user is assigned the same amount of power from  $P_t$ , we can obtain the formula of the Location-Based Signal-to-Leakage-plus-Noise ratio (LB-SLNR) beamformer  $\widehat{\mathbf{W}}_p$ , by normalizing the columns of the LB-MMSE beamformer as follows:

$$\widehat{\mathbf{W}}_{p} = \frac{1}{\sqrt{N}} \mathbf{W}_{p} (\operatorname{diag}(\operatorname{diag}(\mathbf{W}_{p}^{H} \mathbf{W}_{p})))^{-1/2}$$
(3.21)

In subsequent steps, the matrix is normalized depending on the applied constraint:

• SPC (Sum-Power Constraint): normalization ensures that the total transmit power across all antennas does not exceed  $P_t$ .

$$\widetilde{\mathbf{W}}_{p}^{(\mathrm{SPC})} = \frac{\sqrt{P_{t}} \, \widehat{\mathbf{W}}_{p}}{\sqrt{\mathrm{tr}(\widehat{\mathbf{W}}_{p} \widehat{\mathbf{W}}_{p}^{H})}}$$

• PAC (Per-Antenna Constraint): normalization is performed on each antenna branch, guaranteeing that no antenna transmits beyond its hardware limit.

$$\widehat{\mathbf{W}}_{p}^{(\mathrm{PAC})} = \sqrt{\frac{P_{t}}{N}} \left( \mathrm{diag} \left( \mathrm{diag} (\widehat{\mathbf{W}}_{p} \widehat{\mathbf{W}}_{p}^{H}) \right) \right)^{-\frac{1}{2}} \widehat{\mathbf{W}}_{p}$$

The algorithm outputs the final beamforming matrices  $\widetilde{\mathbf{W}}_{p}^{(SPC)}$  and  $\widetilde{\mathbf{W}}_{p}^{(PAC)}$ , which are subsequently used for multi-user transmission.

This approach extends plain beam steering, where the precoder would simply be aligned with the channel vector of each user. As a result, although more complex, LB-MMSE significantly improves SINR, throughput, and fairness in clustered multi-user NTN scenarios.

#### 3.4.2 Plain Beam-Steering

The plain beam-steering approach corresponds to a Matched Filter (MF) beamforming strategy, where the beam for each user is steered towards the direction of its angular position in terms of elevation angle  $\vartheta_k$  and azimuth  $\varphi_k$ , without explicitly mitigating multi-user interference. For each user k, the array steering vector  $a_{UPA}(\vartheta_k, \varphi_k)$ , is defined as:

$$\mathbf{a}_{UPA}(\vartheta_k, \varphi_k) = \mathbf{a}_H(\vartheta_k, \varphi_k) \otimes \mathbf{a}_V(\vartheta_k)$$
(3.22)

Where  $\mathbf{a}_H(\vartheta_k, \varphi_k) \in \mathbb{C}^{1 \times N_H}$  is the horizontal steering vector and similarly  $\mathbf{a}_V(\vartheta_k) \in \mathbb{C}^{1 \times N_V}$  is the vertical steering vector.

The resulting steering vector  $\mathbf{a}_{UPA}(\vartheta_k, \varphi_k) \in \mathbb{C}^{1 \times N}$  is then used to form the  $N \times 1$  Matched Filter beamforming vector  $\mathbf{w}_k^{MF}$ , where  $N = N_H \times N_V$  is the total number of antenna elements:

$$\mathbf{w}_{k}^{MF} = \frac{1}{\sqrt{N}} \mathbf{a}_{UPA}^{H}(\vartheta_{k}, \varphi_{k}) \tag{3.23}$$

Finally, the full matched filtering beamforming matrix of the p-th cluster with  $K_p$  users,  $w_p^{MF} \in \mathbb{C}^{N \times K_p}$ , is constructed by stacking the normalized conjugate steering vectors for all  $K_p$  users as columns:

$$\mathbf{w}_p^{MF} = [\mathbf{w}_1^{MF}, \mathbf{w}_2^{MF}, \dots, \mathbf{w}_{K_p}^{MF}]$$
(3.24)

#### Algorithm 1 Beamforming LB-SLNR

#### Input:

Total inferred channel matrix  $\widehat{\mathbf{H}} \in \mathbb{C}^{N \times K}$ Cluster sets  $\mathcal{C}_p$ , and cluster sizes  $K_p$ ,  $\forall p$ Transmit power  $P_t$   $\triangleright N$  number of antennas

#### **Output:**

Beamforming matrices  $\widetilde{\mathbf{W}}_{p}^{(\mathrm{SPC})}$  and  $\widetilde{\mathbf{W}}_{p}^{(\mathrm{PAC})}$ ,  $\forall p$ 

1: **for** 
$$p := 1$$
 **to**  $P$  **do**

2: 
$$\widehat{\mathbf{H}}_p = \widehat{\mathbf{H}}(\mathcal{C}_p,:)$$

3:  $\alpha_p \leftarrow K_p/P_t \triangleright \text{Regularization factor } \alpha_p \text{ based on number of users } K_p \text{ in the } p\text{-th cluster and transmit power } P_t$ 

4: 
$$\mathbf{W}_p \leftarrow \widehat{\mathbf{H}}^H \left(\widehat{\mathbf{H}}_p \widehat{\mathbf{H}}_p^H + \alpha_p \mathbf{I}_{K_p}\right)^{-1}$$
  $\triangleright \mathbf{I}_{K_p}$  identity matrix of size  $K_p \times K_p$ 

5:  $\widehat{\mathbf{W}}_{p} \leftarrow \frac{1}{\sqrt{N}} \widehat{\mathbf{W}}_{p} \left( \operatorname{diag} \left( \operatorname{diag} \left( \mathbf{W}_{p}^{H} \mathbf{W}_{p} \right) \right) \right)^{-1/2} \triangleright \operatorname{Normalization} \text{ of the columns of } \mathbf{W}_{p}$ 

6: 
$$\widetilde{\mathbf{W}}_{p}^{(\mathrm{SPC})} = \sqrt{P_{t}}\widehat{\mathbf{W}}_{p} / \sqrt{\mathrm{tr}(\widehat{\mathbf{W}}_{p}\widehat{\mathbf{W}}_{p}^{H})}$$

7: 
$$\widehat{\mathbf{W}}_{p}^{(\mathrm{PAC})} = \sqrt{\frac{P_{t}}{N}} \widehat{\mathbf{W}}_{p} \left( \operatorname{diag} \left( \operatorname{diag} \left( \widehat{\mathbf{W}}_{p} \widehat{\mathbf{W}}_{p}^{H} \right) \right) \right)^{-\frac{1}{2}} \widehat{\mathbf{W}}_{p}$$
 > Normalization of the rows of  $\widehat{\mathbf{W}}_{p}$ 

8: end for

This matrix is then used to generate the transmit signal for the users in cluster p.

### Chapter 4

## User Scheduling Algorithms

As discussed previously, the users are grouped into clusters and each cluster is served via TDMA, while users within the cluster are then served simultaneously via SDMA. This scenario is shown in Figure 4.1.

Scheduling one extra group requires one extra time slot, which would lead to groups being served less frequently, reducing the data rate for each group. Therefore, to guarantee the basis for high data rates for each group, the number of groups (consequently of time slots) should be fixed to P. However, fixing the number of groups while respecting the constraints of the algorithms, would lead to some users not being scheduled. In this work, we propose solutions in order to achieve a complete user scheduling, in a fixed number of time slots P.

Given a total scheduling time frame  $T_{sch}$ , each cluster is assigned a time slot  $T_p$ , where  $p \in [1, P]$ . In order to design a fair-proportional scheduler, it is assumed that the duration of each time slot  $T_p$  can be adjusted to mirror the time needed to serve all users within that cluster. In essence, assuming that  $K_p$  is the cardinality of cluster p, or the number of users in that cluster,  $T_p$  can be a multiple of  $T_{sch}$  and an additional quantity  $\gamma_p$ , where  $\gamma_p$  is the ideal cluster weight:

$$\gamma_p = \frac{K_p}{\sum_{p=1}^P K_p} = \frac{K_p}{K}$$

In real communication systems,  $T_p$  cannot be chosen arbitrarily, hence we assume that  $T_p$  is a multiple of the fundamental time slot unit (or minimum allocable time slot)  $T_u$ :

$$T_p = n_p T_u$$

Given the proportional-fair scheduling design, we set  $n_p$  as:

$$n_p = \left\lfloor \frac{\gamma_p \, T_{\text{sch}}}{T_u} \right\rfloor \in \mathbb{Z}^+ \tag{4.1}$$

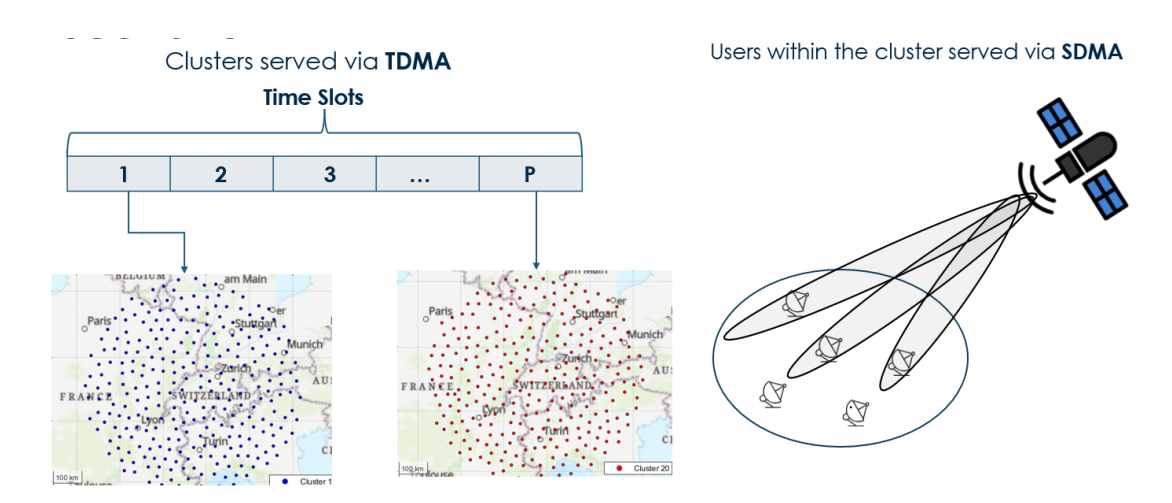
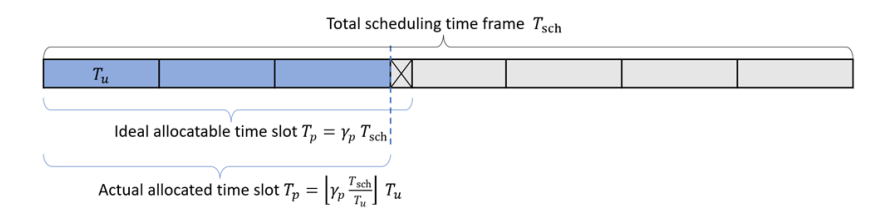


Figure 4.1: Time and Space Division for Multi-User Access in NTN



**Figure 4.2:** Discretized time allocation for cluster p within the scheduling frame  $T_{sch}$ .

Therefore, the actual cluster weight  $\hat{\gamma}_p$  becomes:

$$\hat{\gamma}_p = \frac{n_p T_u}{T_{\text{sch}}} \tag{4.2}$$

This ensures that the allocated time  $T_p$  is a multiple of the time unit  $T_u$ , while remaining proportional to the cluster's relative user load, as illustrated in Figure 4.2.

Once the time slots  $T_p$  are allocated proportionally to cluster load, the next step is to determine how users within each cluster are simultaneously served during their assigned slot. This intra-cluster user selection is critical for maximizing spatial multiplexing gains, especially under SDMA. To achieve this, different user scheduling algorithms can be applied depending on the available information and system constraints. The user scheduling algorithms considered in this work are either CSI-based (MADOC) or Location-based (Distance based MADOC, D-MCC-DSatur and Heuristic RRM)

#### 4.1 MADOC

The first algorithm considered, Multiple Antenna Downlink Orthogonal Clustering, or MADOC [7], groups users in the same cluster considering channel correlation via a Coefficient of Correlation (CoC). CoC indicates the interference user i has on user j, by considering the orthogonality of their channel vectors:

$$\operatorname{CoC}(i,j) = \cos\left(\angle(\mathbf{h}_i, \mathbf{h}_j)\right) = \frac{\left|\mathbf{h}_i^H \mathbf{h}_j\right|}{\|\mathbf{h}_i\| \|\mathbf{h}_j\|} < \epsilon_c, \quad \forall i \neq j \mid i, j \in \mathcal{C}_p, \ 1 \leq p \leq P$$
(4.3)

The clustering process starts by estimating the minimum number of groups required so that each group can contain up to  $N_F$  users, where  $N_F$  is the number of satellite feeds or transmit antennas. Each group is then initialized with one user, selected as the user with the highest channel norm  $\|\mathbf{h}_k\|$ , which represents the strongest link to the satellite. This step ensures that the most dominant users are distributed across different clusters, preventing high-power users from interfering with each other when served simultaneously.

Subsequently, the remaining users are assigned iteratively to the group where their addition causes the smallest degradation in channel orthogonality, as measured by the maximum CoC value between their channel and those already in the group. If this value remains below the threshold  $\epsilon_c$ , the user is added to that cluster; otherwise, a new cluster is created for that user. Algorithm 2 shows the pseudocode for the original MADOC algorithm.

As mentioned before, if this interference is lower than a threshold  $\epsilon_c$ , the users are placed together in a cluster and served via SDMA. Imposing this hard condition on the CoC would lead to some users being unscheduled, as not all users would be able to satisfy it. Therefore, to achieve fixed cluster allocation, i.e. ensuring all users are scheduled, each user is assigned to the cluster that minimizes the maximum interference to its members.

$$s = \arg\min_{p} \left( \max_{j \in C_p} \operatorname{CoC}(i, j) \right), \quad 1 \le p \le P$$
 (4.4)

#### 4.2 D-MADOC

D-MADOC [8] is a location-based version of the original MADOC [7]. In this distance-based version,  $Q = \left\lceil \frac{K}{N} \right\rceil < P$  groups are initialized so that each group initially contains only one of the Q users with the shortest slant range. Then, the remaining users are sorted in order of increasing slant range, and each of them is assigned to a group according to the great-circle distance (GCD) matrix  $\Gamma$ . In 4.5,

#### **Algorithm 2** MADOC Algorithm

```
▷ Initial estimate of the number of user groups based on total users and
1: N_G = |
    available feeds
2: K = \{1, 2, \dots, K_{\text{tot}}\}
                                                                               ▶ Initialize the full set of user indices
                                                                   \triangleright Initialize all N_G user groups as empty sets
3: \mathcal{T}(1) = \ldots = \mathcal{T}(N_G) = \emptyset
4: for g = 1 to N_G do
                                         ▷ Select the user with the strongest channel norm (best link)
    u = \arg\max_{u} \|\mathbf{h}_{u^*}\|
                                                                  \triangleright Assign this user as the first user of group g
      \mathcal{T}(g) = \{u\}
      \mathcal{K} = \mathcal{K} \setminus \{u\}
                                                           ▶ Remove selected user from the unassigned pool
8: end for
9: while |\mathcal{K}| > 0 do
                                                                         ▶ Pick the next strongest remaining user
       u = \arg\max_{u^* \in \mathcal{K}} \|\mathbf{h}_{u^*}\|
       g_s = rg \min_{1 \leq g \leq N_G} \left( \max_{i \in \mathcal{T}(g)} \cos \left( \angle (\mathbf{h}_u, \mathbf{h}_i) \right) \right)
                                                                         \triangleright Find the group where u has the lowest
    maximum spatial correlation (best angular separation)
       if \max_{i \in \mathcal{T}(g_s)} \cos(\angle(\mathbf{h}_u, \mathbf{h}_i)) < \epsilon then
12:
13:
          \mathcal{T}(g_s) = \mathcal{T}(g_s) \cup \{u\} \triangleright \text{Add } u \text{ to group } g_s \text{ if its channel is sufficiently orthogonal to all }
    group members
14:
15:
                                                                             \triangleright Otherwise, create a new group for u
           N_G = N_G + 1
16:
                                                                          ▶ Initialize the new group with this user
          \mathcal{T}(N_G) = \{u\}
        end if
17:
                                                                        \triangleright Remove user u from the candidate pool
18:
       \mathcal{K} = \mathcal{K} \setminus \{u\}
19: end while
```

the pair  $(\xi_i, \lambda_i)$  represents the latitude and the longitude of user i and similarly  $(\xi_j, \lambda_j)$  represents the latitude and longitude of user j.

$$[\mathbf{\Gamma}]_{i,j} = 2r \sin^{-1} \left( \sqrt{\sin^2 \left( \frac{\xi_j - \xi_i}{2} \right) + \cos \xi_i \cos \xi_j \sin^2 \left( \frac{\lambda_j - \lambda_i}{2} \right)} \right) > \epsilon_d \qquad (4.5)$$

If the distance between users i and j represented by  $[\Gamma]_{i,j}$  is larger than the threshold  $\epsilon_d$ , users are considered to be "distant enough" and are scheduled together. If this is not the case, a new cluster is created for user i, as long as there are less than P clusters already created.

Algorithm 3 shows the pseudocode for the algorithm.

Just like for the original MADOC, in order to schedule all users in a limited number of groups P, a slight modification is needed. In this case, a user is placed in the cluster s with the maximum minimum distance, i.e., where the closest neighbour is the furthest, according to the expression 4.6.

$$s = \arg\max_{p} \left( \min_{j \in C_p} [\Gamma]_{i,j} \right), \quad 1 \le p \le P$$
 (4.6)

#### **Algorithm 3** D-MADOC Algorithm

```
Input:
       Set of all users to be scheduled \mathcal{U} = \{U_1, U_2, \dots, U_K\}
       Total number of feeds N
       Vector of users' slant ranges \mathbf{d} = [d_1, d_2, \dots, d_K]
       Users' great circle distance matrix \Gamma
       Cluster sets C_p
       Cluster weights \gamma_p, for p = 1, \dots, P
 1: K \leftarrow |\mathcal{U}|
 2: \mathcal{R} \leftarrow \mathcal{U}
 3: P \leftarrow \left\lfloor \frac{K}{N} \right\rfloor
 4: Initialize \tilde{\mathcal{C}}_1 = \mathcal{C}_2 = \ldots = \mathcal{C}_P = \varnothing
 5: for p = 1 to P do
         v = \arg\min_{i \in \mathcal{I}} d_i
          \mathcal{C}_p \leftarrow \{v\}
         \mathcal{R} \leftarrow \mathcal{R} \setminus \{v\}
 9: end for
10: while \mathcal{R} \neq \emptyset do
11:
          v = \arg\min_{i} d_i
            s = \arg \max_{1 \le p \le P} \left( \min_{u_j \in \mathcal{C}_p} |\mathbf{\Gamma}_{i,j}| \right)
12:
            if \min_{u_j \in \mathcal{C}_s} |\mathbf{\Gamma}_{i,j}| > C_D then
13:
                \mathcal{C}_s \leftarrow \mathcal{C}_s \cup \{v\}
15:
            else
16:
                P \leftarrow P + 1
               C_P \leftarrow \{v\}
17:
18:
            end if
19:
           \mathcal{R} \leftarrow \mathcal{R} \setminus \{v\}
20:
           p \leftarrow p + 1
21: end while
22: for p = 1 to P do
         K_p \leftarrow |\mathcal{C}_p| \atop K_p
23:
                       \frac{\prod_{r=1}^{P} K_r}{\sum_{r=1}^{P} K_r}
25: end for
```

#### 4.3 D-MCC-DSatur

D-MCC-DSatur is another location-based user scheduling algorithm. It deploys a graph coloring strategy in a greedy manner, where a color cannot be assigned to two adjacent nodes. In this case, the user scheduling problem is modeled using an undirected, unweighted graph  $\mathcal{G} = (\mathcal{V}, \mathcal{E})$ , where each vertex  $v \in \mathcal{V}$  represents a user, and an edge  $\varepsilon \in \mathcal{E}$  represents users that are co-schedulable. The graph is created by considering the inter-user distance  $[\Gamma]_{i,j}$ : if two users (nodes) are geographically 'distant enough', an edge is drawn between them, according to the expression 4.7.

$$\exists \varepsilon(i,j) \text{ if } [\Gamma]_{i,j} \geq \delta_d, \quad [\Gamma]_{i,j} : \text{geographical distance metric } 4.5$$
 (4.7)

The objective is to minimize the number of clusters, which is equivalent to solving the Minimum Clique Cover (MCC) problem on  $\mathcal{G}$ , where a clique is a completely connected sub-graph. In [38], the MCC problem is approached by mapping it into a graph coloring problem on the complementary graph  $\bar{\mathcal{G}}$ , whose adjacency matrix is defined as:

$$[\bar{\mathbf{A}}]_{i,j} = \begin{cases} 1 & \text{if } [\Gamma]_{i,j} \le \delta_d \\ 0 & \text{otherwise} \end{cases}$$
 (4.8)

Since resolving this problem is generally NP-hard, the scheduler makes use of a heuristic method, the original DSatur algorithm [43], which iteratively selects the next vertex with the highest number of distinct colored neighbors (i.e., highest saturation degree).

In order to respect the threshold condition, the algorithm creates the necessary number of clusters, which may be larger than P, but ultimately considers only the largest P clusters. To assign all unassigned users to these P clusters, aiming to balance the size of the clusters while still respecting (to some extent) the condition on the minimum inter-user distance, we adopt the same criterion used in D-MADOC (4.6). The complete scheduling algorithm is reported in Algorithm 4. The scheduling procedure makes use of the 'FindCandidateNode' function reported in Algorithm 5.

#### 4.4 Heuristic-RRM

Heuristic-RRM considers as input the matrix  $\mathbf{Q}$ , briefly defined as the interference matrix, the maximum number of time slots/groups, and the total number of users K to be scheduled. As the number of time slots is provided as input to the algorithm, no modifications are needed to fix or set the number of time slots.

The interference matrix  $\mathbf{Q}$  is derived from the power transfer matrix  $\mathbf{S}$ , whose elements s(i,j) describe the power transmitted for user j and received by user i. From  $\mathbf{S}$ ,  $\mathbf{Q}$  can be derived by nulling the diagonal elements, as a user does not interfere with itself. Conceptually, at each step the algorithm tries to evaluate the interference each user could cause to every other user if they were grouped together.

The important concept behind the algorithm is that it makes use of the approximated evaluation of the power transfer matrix, instead of computing exact power "leakage". Computing exact interference values can be computationally

intensive and depend on the antenna patterns. Instead, the model considers mainly the interference from the main beam and approximates it using a Gaussian beam pattern:

$$g_0(u,v) = \exp\left(-\frac{1}{2\sigma^2}(u^2 + v^2)\right), \quad v: \text{ user's direction cosines.}$$
 (4.9)

The parameter  $\sigma$  can be tuned to match the main beam of the considered antenna, mainly by considering  $D_A$ , the antenna aperture size, given as the product between the number of elements and the spacing between the elements in that direction:

$$D_A = d_H \times N_H = d_V \times N_V \tag{4.10}$$

Using this approximation allows the algorithm to evaluate the co-channel interference by simply using the users' locations. The interference from user j to user i can be estimated as:

$$q(i,j) = \left| g_0(\Delta u, \Delta v) \right|^2 = \exp\left( -\frac{1}{\sigma^2} \left( (u_i - u_j)^2 + (v_i - v_j)^2 \right) \right)$$
(4.11)

The elements of  $\mathbf{Q}$ , i.e. q(i,j), are values between 0 and 1 and essentially represent the interference power between two users.

The algorithm first starts by selecting the first user to assign. This user is chosen as the one showing the highest value in the  $\mathbf{Q}$  matrix, i.e. the user with the worst interference.

Next, the algorithm considers an auxiliary co-channel interference matrix  $\mathbf{A}$ , which provides information about the interference on a user due to all the users who have been assigned to cluster p.

$$\mathbf{A} = \mathbf{QC} \tag{4.12}$$

The element  $[\mathbf{A}]_{k,p}$  quantifies the total interference experienced by user k if it were to be assigned to cluster p. The algorithm then finds, among the unassigned users, the user with the worst aggregated interference, by looking at the row with the maximum value across all clusters.

For this user, the selected cluster is the one with the least aggregated interference. The user is assigned to the selected cluster, marked as assigned, the matrix  $\mathbf{A}$  is updated, and the loop repeats to select the next user and their best cluster, until all users have been scheduled.

A detailed overview of the algorithm is shown in the pseudocode Algorithm 6.

#### Algorithm 4 D-MCC-DSatur algorithm

```
Input:
     Set of all users to be scheduled \mathcal{U} = \{U_1, U_2, \dots, U_K\}
     Great-Circle Distance matrix \Gamma
     Graph threshold \delta_D
     P, Number of clusters to create, i.e., number of time slots
Output:
     Cluster sets C_p
     Cluster weights \gamma_p for p = 1, \ldots, P
 1: K \leftarrow |\mathcal{U}|
 2: \bar{\mathbf{A}} \leftarrow \mathbf{0}_{K \times K}
 3: for i, j := 1 to K do
      if \Gamma(i,j) < \delta_D then
 5:
           \bar{\mathbf{A}}(i,j) = 1
                                                            \triangleright Build adjacency matrix of the complement graph \mathcal{G}_c
 6:
        end if
 7: end for
                                                                         ▶ Ensure no self loops are present in the graph
 8: \bar{\mathbf{A}}(i,i) = 0, \ \forall i
9: \{C_1, C_2, \dots, C_Q\} \leftarrow DSatur(\bar{\mathbf{A}}, K)
10: if Q > P then
                                                                         \triangleright Q total number of formed clusters by DSatur
11: Sort clusters C_q, q = 1, ..., Q, by decreasing size
12:
        Keep only the first P clusters C_1, \ldots, C_P
13: end if
14: \mathcal{N} \leftarrow \{U_i \in \mathcal{U} \mid U_i \notin \bigcup_{p=1}^P \mathcal{C}_p\} belonging to any \mathcal{C}_p
                                                                 \triangleright Initialize set of unscheduled users, i.e. any U_i not
15: while \mathcal{N} \neq \emptyset do
16: Select U_i from \mathcal{N}
         s = \operatorname*{arg\,max}_{1 \leq p \leq P} \left( \min_{U_j \in \mathcal{C}_p} \left[ \mathbf{\Gamma} \right]_{i,j} \right) \rhd \text{ For each cluster } \mathcal{C}_p, \text{ find the user } U_j^{(p)} \text{ at minimum distance,}
     then select the cluster s with U_i^{(s)} at maximum distance
       C_s \leftarrow C_s \cup \{U_i\}\mathcal{N} \leftarrow \mathcal{N} - \{U_i\}
                                                                                                                                         \triangleright Update \mathcal{N}
19:
20: end while
21: for p := 1 to P do
                                                                                                                            ▷ Cluster weighting
21: for p...
22: K_p \leftarrow |\mathcal{C}_p| K_p
             \leftarrow \frac{K_p}{\sum_{p=1}^P K_p}
24: end for
     Function \{C_1, \ldots, C_Q\} = \mathrm{DSatur}(\bar{\mathbf{A}}, K)
25: Generate graph \mathcal{G}_c(\mathcal{U}, \mathcal{E}), with vertex set \mathcal{U} and edge set \mathcal{E}, where \{U_i, U_j\} \in \mathcal{E} if \bar{\mathbf{A}}(i, j) = 1
26: for each vertex v \in \mathcal{U} do
                                      \triangleright \mathcal{S}(v) is the set of the distinct colors assigned to neighbors of (v)
27: S(v) \leftarrow \emptyset
                                                     \triangleright number of distinct colors assigned to the neighbors of v,
      Saturation(v) \leftarrow 0
     Saturation(v) = |\mathcal{S}(v)|
29: degree(v) \leftarrow \sum_{i=1}^{K} \bar{\mathbf{A}}(v, i)
30: end for
31: while \mathcal{U} \neq \emptyset do
                                                                                                                                    ▶ Algorithm 5
32:
         v = \text{FindCandidateNode}(\mathcal{U})
33:
         if v is not colored then
             q = \max_{x \in \mathcal{X}} + 1 \triangleright Assign smallest color not used by neighbors of v, if \mathcal{S}(v) = \emptyset, then
34:
35:
            \mathcal{C}_q \leftarrow \mathcal{C}_q \cup v
36:
             for each neighbor w of v do
37:
                if w is not colored and q \notin S(v) then
38:
                   Saturation(w) \leftarrow Saturation(w) + 1
39:
                   degree(w) \leftarrow degree(w) - 1
                                                     \triangleright Add q to the set of the distinct colors of neighbors of w
40:
                   \mathcal{S}(w) \leftarrow \mathcal{S}(w) \cup q
41:
                end if
                                                                             33
42:
             end for
43:
            \mathcal{U} \leftarrow \mathcal{U} - \{v\}
         end if
45: end while
```

#### Algorithm 5 FindCandidateNode Function

```
1: n \leftarrow \max_{v \in \mathcal{U}} (\text{Saturation}(v))
2: Q \leftarrow \{v \in \mathcal{U} \mid \text{Saturation}(v) = n\} \triangleright Q is the set of users with the same maximum saturation
3: if |Q| = 1 then
4: return v \in \mathcal{Q}
5: else if |Q| > 1 then
6: m \leftarrow \max_{w \in \mathcal{Q}} (\text{degree}(w))
   \mathcal{Z} \leftarrow \{w \in \mathcal{Q} \mid \text{degree}(w) = m\} \triangleright \mathcal{Z} is the set of users with the same maximum saturation and same maximum degree
8: if |Z| = 1 then
9:
          return w \in \mathcal{Z}
10:
        else if |Q| > 1 then
11:
          return the first element of \mathcal{Z} or break the tie arbitrarely
12: end if
13: end if
```

#### Algorithm 6 Heuristic RRM Algorithm

#### Input:

Q, Interference matrix

 $\triangleright \mathbf{Q} \in K \times K$ 

P, Number of clusters to create, i.e., number of time slots

K, Total number of users

#### Output:

C, Clustering matrix

 $\triangleright$  Binary matrix  $\mathbf{C} \in K \times P$ 

Cluster weights  $\gamma_p$  for  $p = 1, \dots, P$ 

1: 
$$\mathbf{Q}(k,k) \leftarrow 0, \ \forall k$$

▶ Null diagonal

2:  $\mathbf{C} \leftarrow \mathbf{0}_{K \times P}$ 

3:  $\mathbf{A} \leftarrow \mathbf{0}_{K \times P}$ 

▶ Aggregate interference matrix

 $\triangleright$  Remove user  $k^{(1)}$  from the list

4:  $\mathbf{u} \leftarrow \mathbf{0}_{K \times 1}$   $\triangleright \mathbf{u}$  is a  $K \times 1$  Boolean vector, u(k) = 1 if user k has been scheduled

5:  $k^{(1)} \leftarrow \arg\max_{k} \left[ \arg\max_{p} \mathbf{Q}(k, p) \right] \triangleright \text{Find user with worst single-entry interference}$ 

6:  $\mathbf{C}(k^{(1)}, 1) \leftarrow 1$ 

 $\triangleright$  Assign user  $k^{(1)}$  to the first cluster

7:  $\mathbf{u}(k^{(1)}) \leftarrow 1$ 

8:  $\mathbf{A}(:,1) \leftarrow \mathbf{Q}(:,k^{(1)})$ 

9: while  $\|\mathbf{u}\|_1 < K$  do

 $\mathbf{b} \|\mathbf{u}\|_1 = \sum_{k=0}^K |u(k)|$  is the 1-norm of a vector

10:  $k^{(i)} \leftarrow \underset{k,\mathbf{u}(k)=0}{\operatorname{arg max}} \left[ \underset{p}{\operatorname{arg max}} \mathbf{A}(k,p) \right]$   $\triangleright$  Find user with worst single-entry

interference

11:  $p^{(i)} \leftarrow \underset{p}{\operatorname{arg\,min}} \mathbf{A}(k^{(i)}, p)$   $\triangleright$  Find cluster with least aggregated interference

12:  $\mathbf{C}(k^{(i)}, p^{(i)}) \leftarrow 1$ 

 $\triangleright$  Assign user  $k^{(i)}$  to cluster  $p^{(i)}$ 

13:  $\mathbf{u}(k^{(i)}) \leftarrow 1$ 

 $\triangleright$  Remove user  $k^{(i)}$  from the list

14:  $\mathbf{A}(:, p^{(i)}) \leftarrow \mathbf{A}(:, p^{(i)}) + \mathbf{Q}(:, k^{(i)})$ 

15: end while

16: **for** p := 1 **to** P **do** 

▷ Cluster weighting

17:  $K_p \leftarrow |\mathcal{C}_p|$ 

18:  $\gamma_p \leftarrow \frac{K_p}{\sum_{p=1}^P K_p}$ 

19: end for

### Chapter 5

# Results and performance evaluation

This chapter presents the performance evaluation of the proposed user scheduling algorithms under different system assumptions and channel conditions. The analysis is carried out by considering the effect of the transmit power budget, expressed through the Effective Isotropic Radiated Power (EIRP) density, on several key performance indicators (KPIs).

Effective Isotropic Radiated Power (EIRP). The EIRP represents the equivalent radiated power of an isotropic antenna and is defined as the product of the transmitted power  $P_{TX}$  and the antenna gain  $G_a$ :

$$EIRP = P_{TX} \cdot G_{a}, \qquad EIRP_{dB} = P_{TX,dB} + G_{a,dB}$$

For an array of N elements, each with single-element gain  $G_{\text{elem,dB}}$ , the array gain is given by

$$G_{\text{a,dB}} = G_{\text{elem,dB}} + 10 \log_{10}(N).$$
 (5.1)

In this work, the EIRP density (dBW/MHz) is used, obtained by normalizing the EIRP to the system bandwidth. It directly determines the transmitting power (5.2) and therefore influences all the KPIs considered.

$$P_{\text{TX,dB}} = EIRP_{\text{dens,dB}} + 10\log_{10}(B) - G_{a,\text{dB}}$$
 B: system bandwidth (5.2)

**Key Performance Indicators (KPIs).** The performance of the scheduling algorithms is evaluated using the following metrics:

1. Cluster size: the number of users  $K_p$  scheduled in cluster p.

$$|C_p| = K_p$$

2. **SINR:** the signal-to-interference-plus-noise ratio of user k in cluster p:

$$SINR_{k}^{(p)} = \frac{\|\mathbf{h}_{k}\mathbf{w}_{k}^{(p)}\|^{2}}{1 + \sum_{\substack{i=1\\i \neq k}}^{K_{p}} \|\mathbf{h}_{k}\mathbf{w}_{i}^{(p)}\|^{2}}$$

For the calculation of the KPIs, the actual channel  $\mathbf{h}_k$  encountered on the k-th link during propagation is considered, and it is, in general, mismatched with the inferred one  $\hat{\mathbf{h}}_k$ , and consequently with  $\mathbf{w}_k^{(p)}$ .

3. **Per-user throughput:** the achievable rate of user k in cluster p, according to the Shannon formula:

$$R_k = \hat{\gamma}_p B \cdot \log_2 \left( 1 + SINR_k^{(p)} \right) \tag{5.3}$$

where B is the system bandwidth and  $\hat{\gamma}_p$  is the cluster weight (4.2) assigned to cluster p.

4. **Per-cluster sum-rate:** the aggregated throughput of all users in cluster p:

$$\Gamma_p = B \sum_{k=1}^{K_p} \log_2 \left( 1 + SINR_k^{(p)} \right)$$

5. Outage probability: the fraction of users experiencing an SINR below a target threshold  $\gamma_{\rm th}$ .

By jointly considering EIRP density and these KPIs, the analysis highlights the trade-offs among different scheduling algorithms in terms of spectral efficiency, fairness, and robustness. The remainder of this chapter is organized as follows: Section 5.1 analyzes the impact of a uniform user distribution, while Section 5.2 extends the evaluation to a hybrid distribution that better represents dense-urban scenarios.

# 5.1 Impact of Uniform User Distribution on Algorithm Performance

This chapter evaluates the performance of all four algorithms under the hypothesis that the users are uniformly distributed within the coverage area, while analyzing the effect of the EIRP density on the cluster size, throughput, sum-rate, SINR and an additional metric, the outage.

**Table 5.1:** Simulation Parameters.

Parameter	Value
Carrier frequency	20 GHz (Ka band)
System Band	$400 \mathrm{\ MHz}$
Receiver type	VSAT
Receiver antenna gain	39.7  dBi
Noise figure	$1.2~\mathrm{dB}$
Propagation scenario	LOS + NLOS
System scenario	Rural, sub-urban
Total on-board EIRP density	30  dBW/MHz
User density $\rho_{\mathrm{UEs}}$	$0.01 \text{ users/km}^2$
Number of array antenna elements	$16 \times 16$
Antenna element spacing $(d_H = d_V)$	$0.6\lambda$
Maximum off-nadir angle $\eta_{\text{max}}$ of coverage region	$50^{\circ}$
System latency $\Delta \tau$	10  ms
Optimized number of clusters (except H-RRM)	29
Total scheduling time frame $T_{\rm sch}$	2 s
Time slot unit $T_u$	1 ms

# 5.1.1 Performance evaluation with EIRP equal to 30 dB-W/MHz

The input parameters have been summarized in Table 5.1.

In order to evaluate the performance of the scheduling algorithms, the optimal thresholds have been determined iteratively by evaluating the throughput and are summarized in Table 5.2.

The optimization is two-fold. In the first step, the optimal number of time slots for each algorithm was determined heuristically. For this, the number of time slots was varied and the configuration that achieved the highest throughput was selected as optimal. The optimal number of time slots for MADOC, D-MADOC and DSatur was determined to be 29. Note that since H-RRM uses the number of time slots (or groups to be formed) as input, its optimization was done separately, producing the results shown in Table 5.2.

Secondly, the optimal thresholds were determined, for SPC and PAC separately, by fixing the number of time slots and selecting the threshold that yields the largest throughput. Using these optimal thresholds allows for a fair comparison of the algorithms' performance.

As discussed previously, the evaluation of the performance is based on several KPIs. The histograms in Figure 5.1 show the distribution of cluster sizes for each algorithm, and a summary of the mean cluster sizes can be found in Table 5.3. It

Algorithm	Definition of threshold	SPC	PAC
MADOC	CoC	0.5	0.4
D-MADOC	Distance [km]	33	34.5
H-RRM	Nr. of clusters	28	32
D-MCC-DSatur	Distance [km]	48.4	49

**Table 5.2:** Optimal thresholds for each algorithm.

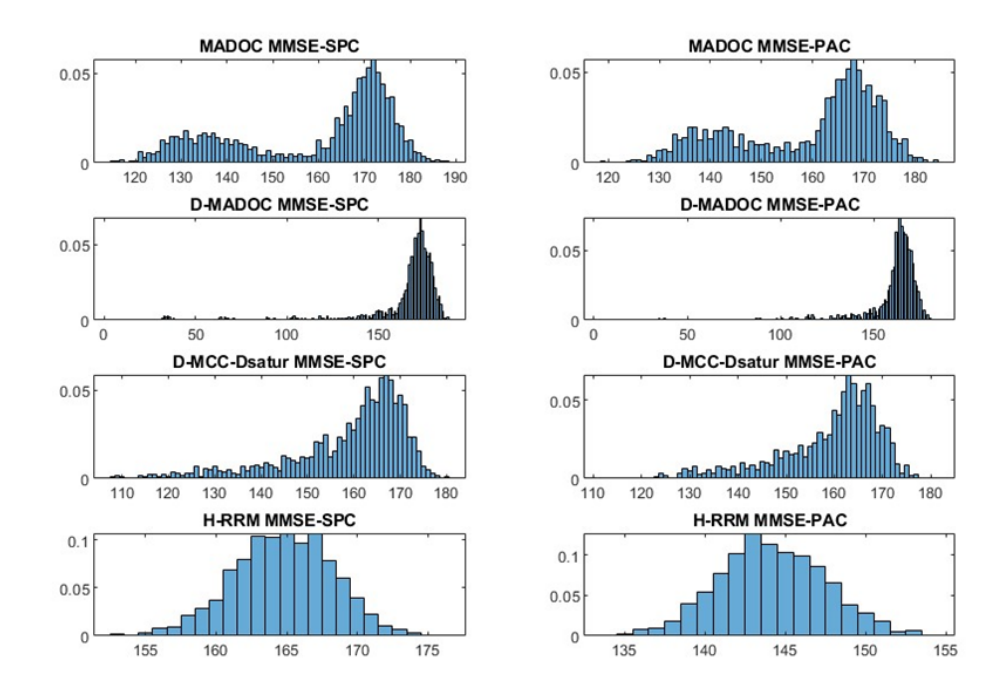


Figure 5.1: Histogram of cluster size distribution for each algorithm.

must be noted that in each case, the number of users per cluster does not surpass the number of elements of the  $16 \times 16$  antenna considered for the scenario.

The results show that the mean cluster size remains relatively constant across all algorithms, demonstrating that all are able to keep a relatively balanced cluster size when scheduling all users.

The performance of the algorithms in terms of **Sum-Rate Capacity** is illustrated in Figure 5.2. It can be seen that MADOC and D-MADOC reach the highest peak capacity (at around 290 Gbps), although only in very limited cases. At lower percentiles, these two algorithms perform poorly, leading to sum-rate capacities below 200 Gbps. This can be attributed to the small clusters these two algorithms create, as shown in the histogram of Figure 5.1. On the other hand,

 Table 5.3: Mean cluster sizes (users/cluster).

Algorithm	SPC	PAC
MADOC	159.08	159.08
D-MADOC	163.96	160.00
D-MCC-DSatur	159.08	159.08
H-RRM	164.76	144.17

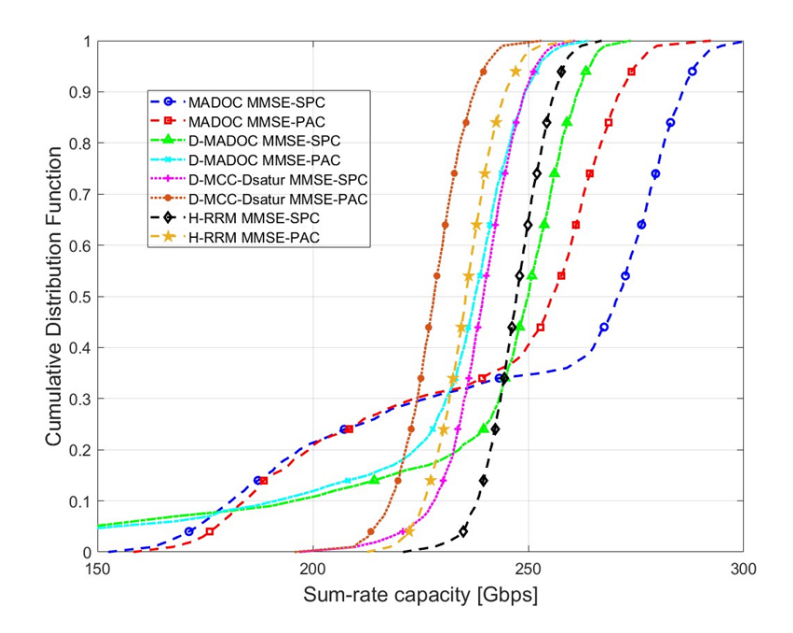


Figure 5.2: Sum-Rate Capacity CDF Comparison Across Algorithms.

D-MCC-DSatur and H-RRM achieve consistently higher and more reliable capacity, typically between 200 and 250 Gbps.

In terms of **SINR** (Figure 5.3), the algorithms show similar distributions. From the figure it can be noted that H-RRM achieves the highest SINR distribution, particularly at lower and middle percentiles. Its median SINR is around 12 dB, which implies better interference management and user separation.

MADOC closely follows H-RRM, with a median SINR of about 11 dB. Despite forming small clusters, MADOC performs well in SINR due to its selection of users based on low channel correlation. This explains its high per-user throughput (as shown later).

D-MADOC and D-MCC-DSatur produce very similar SINR distributions, indicating that while they may not always form the most orthogonal user groups, they maintain consistently good SINR across users.

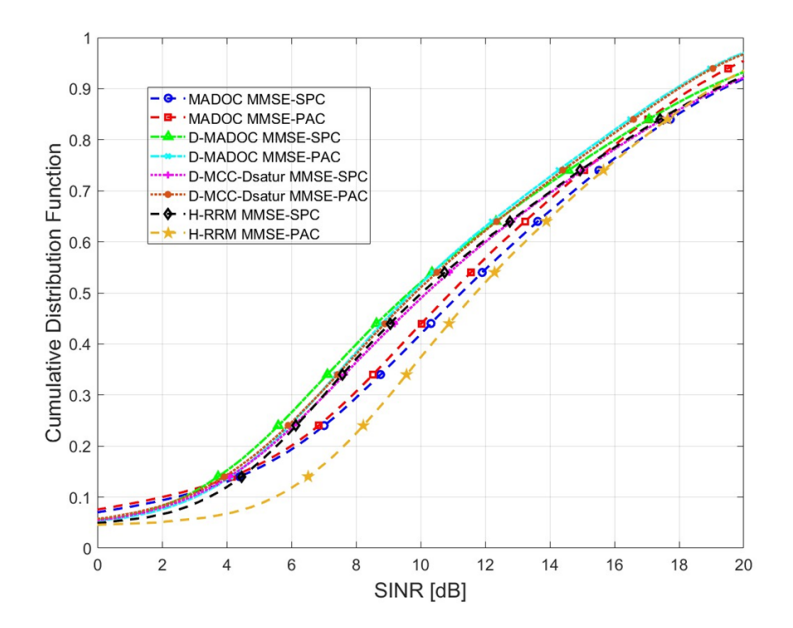


Figure 5.3: SINR CDF Comparison Across Algorithms.

**Table 5.4:** Average metrics of the algorithms at EIRP = 30 dBW/MHz.

	MADOC		D-MADOC D-M		D-MCC	D-MCC-DSatur		H-RRM	
Metric	SPC	PAC	SPC	PAC	SPC	PAC	SPC	PAC	
SINR [dB]	10.564	10.083	9.636	9.504	10.081	9.528	10.097	11.327	
Throughput [Mbps]	54.973	52.625	52.775	59.198	51.862	49.431	53.581	51.034	
Sum-Rate Capacity [Gbps]	249.26	240.08	237.58	228.26	238.85	227.88	247.16	235.40	

Finally, Figure 5.4 shows the performance of the four algorithms in terms of **throughput**. The median throughput across algorithms is around 50 Mbps, with MADOC slightly higher at 53 Mbps, as a direct consequence of its higher SINR, consistent with the logarithmic behavior of the Shannon formula (5.3). H-RRM shows a steeper Cumulative Distribution Function (CDF), suggesting users are served in a fairer manner due to the more consistent cluster sizes. D-MCC-DSatur and D-MADOC follow closely, offering relatively high throughput while maintaining fairness. Table 5.4 reports the average metrics.

#### 5.1.2 Performance evaluation with reduced EIRP

In this section, the EIRP density has been reduced from 30 dBW/MHz to 20 dBW/MHz. The simulation parameters are summarized in Table 5.5.

When the EIRP is reduced, we can expect lower values of SINR, throughput and sum-rate and possibly higher error rates. Looking at Figure 5.5 and comparing

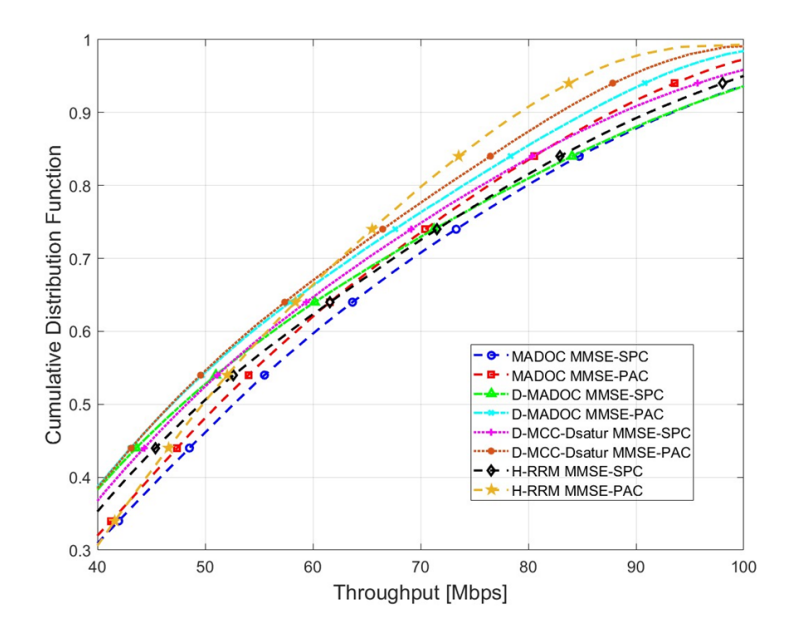


Figure 5.4: Throughput CDF Comparison Across Algorithms.

 Table 5.5: Updated Simulation Parameters.

Parameter	Value
Carrier frequency	20 GHz (Ka band)
System Band	$400 \mathrm{\ MHz}$
Receiver type	VSAT
Receiver antenna gain	$39.7~\mathrm{dBi}$
Noise figure	$1.2~\mathrm{dB}$
Propagation scenario	LOS + NLOS
System scenario	Rural, sub-urban
Total on-board EIRP density	20  dbW/MHz
User density $\rho_{UEs}$	$0.01 \text{ users/km}^2$
Number of array antenna elements	16x16
Antenna element spacing $(d_H = d_V)$	$0.6 \lambda$
Maximum off-nadir angle $\eta_{\rm max}$ of the coverage region	$50^{\circ}$
System latency $\Delta \tau$	10  ms
Total scheduling time frame $T_{sch}$	2 s
Time slot unit $T_u$	1 ms
Outage threshold (minimum SINR)	-6 dB

it to the results of Figure 5.3, we can note that not only is the median reduced,

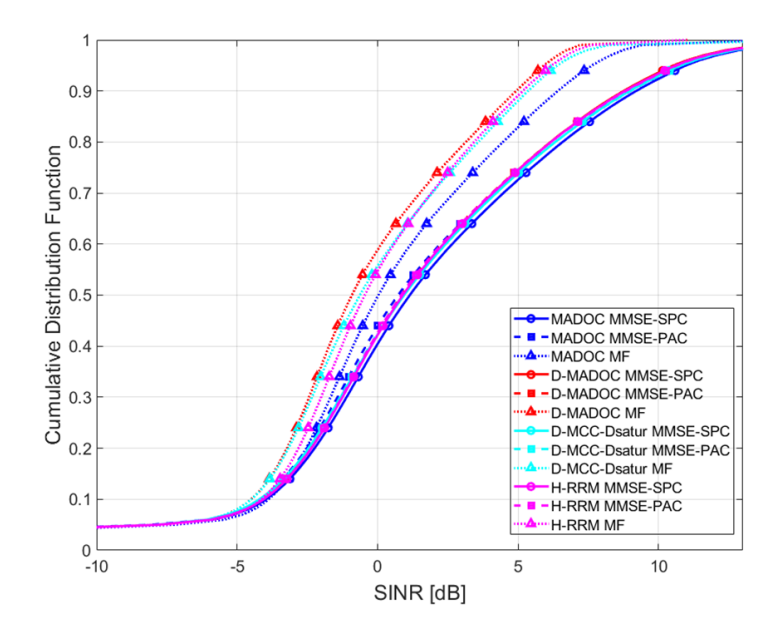


Figure 5.5: Updated SINR CDF Comparison Across Algorithms.

but the set of users that see a very low value of SINR (-10-0 dB) is increased. When translated into the rate according to the Shannon formula (5.3), it means that almost 20% of the users see an uncoded spectral efficiency that corresponds to less than 1 bps/Hz. To avoid biasing the optimization process due to the presence of these unusable links, we adopted the following strategy: in this work, a user is considered to be in **outage** if their SINR falls below -6 dB. These users are assumed to be unable to maintain a stable connection and are therefore excluded from the computation of performance metrics such as average throughput and sum-rate. To still account for their presence in the system, we introduce an additional metric: **the outage percentage**.

In this section, the optimization follows the same approach as in previous analyses, focusing on maximizing the per-user achievable throughput, but now also taking into account the outage percentage. As previously discussed, the optimization process includes a constraint that limits the percentage of users in outage, i.e., those with SINR below -6 dB. During preliminary simulations, it was observed that targeting full user coverage as done previously was not feasible for most algorithms. Some users consistently experienced very poor link conditions ( and these were mainly NLOS users), making them unschedulable. Further experiments revealed that, among all algorithms tested, only H-RRM could achieve a throughput-optimal configuration while keeping the outage rate below 5%. The other algorithms were unable to meet this stricter constraint. As a result, we propose using a 6% outage

**Table 5.6:** Updated optimal thresholds for each algorithm.

Algorithm	Definition of threshold	LB-SLNR-SPC	LB-SLNR-PAC	MF
MADOC	CoC	0.35	0.33	0.33
D-MADOC	Distance [km]	31	31	32.5
D-MCC-DSatur	Distance [km]	44.5	44.5	40

**Table 5.7:** Optimal number of clusters for each algorithm.

Algorithm	LB-SLNR-SPC	LB-SLNR-PAC	MF
MADOC	26	25	25
D-MADOC	26	26	22
H-RRM	25	25	23
D-MCC-DSatur	26	26	24

limit represented by the red dashed line in Figure 5.9, as a practical and fair target. This value provides a balance between performance and coverage, and was found to be achievable by all algorithms across beamforming configurations during the optimization phase.

The optimal number of clusters (or time slots) required for each algorithm to achieve optimal performance was determined through experimental analysis, where each algorithm iterated over a broad range of cluster sizes in order to identify the configuration that maximized the throughput. This optimization process, as in the previous case, is twofold, focusing both on the threshold and the number of clusters. To provide a clearer understanding of how each algorithm performs, we present detailed 3D plots (Fig. 5.6, Fig. 5.7, and Fig. 5.8) that illustrate the relationship between throughput, threshold and cluster size. In these plots, the red marker specifically highlights the optimal combination of threshold and cluster size that each algorithm selects as yielding the best performance.

A 2D representation can be found on the plots of Figure 5.9, where the blue diamond marker indicates the threshold value corresponding to the maximum average throughput constrained to outage below 6%. Moreover, the legends of the plots also present the optimal number of time slot for each beamforming method. A summary of the threshold values follows in Table 5.6.

Specifically for H-RRM, the key parameter to optimize is the number of clusters, which serves as its threshold. To identify the optimal configuration, we vary the number of clusters and select the one that yields the highest throughput. The optimal number of clusters was found to be 25 for both the SPC and PAC variants, and 23 for the Matched Filtering case. Given that the user density remains constant, reducing the number of clusters from 25 to 23 implies that each cluster must contain more users on average. This effect is reflected in the cluster size distribution shown

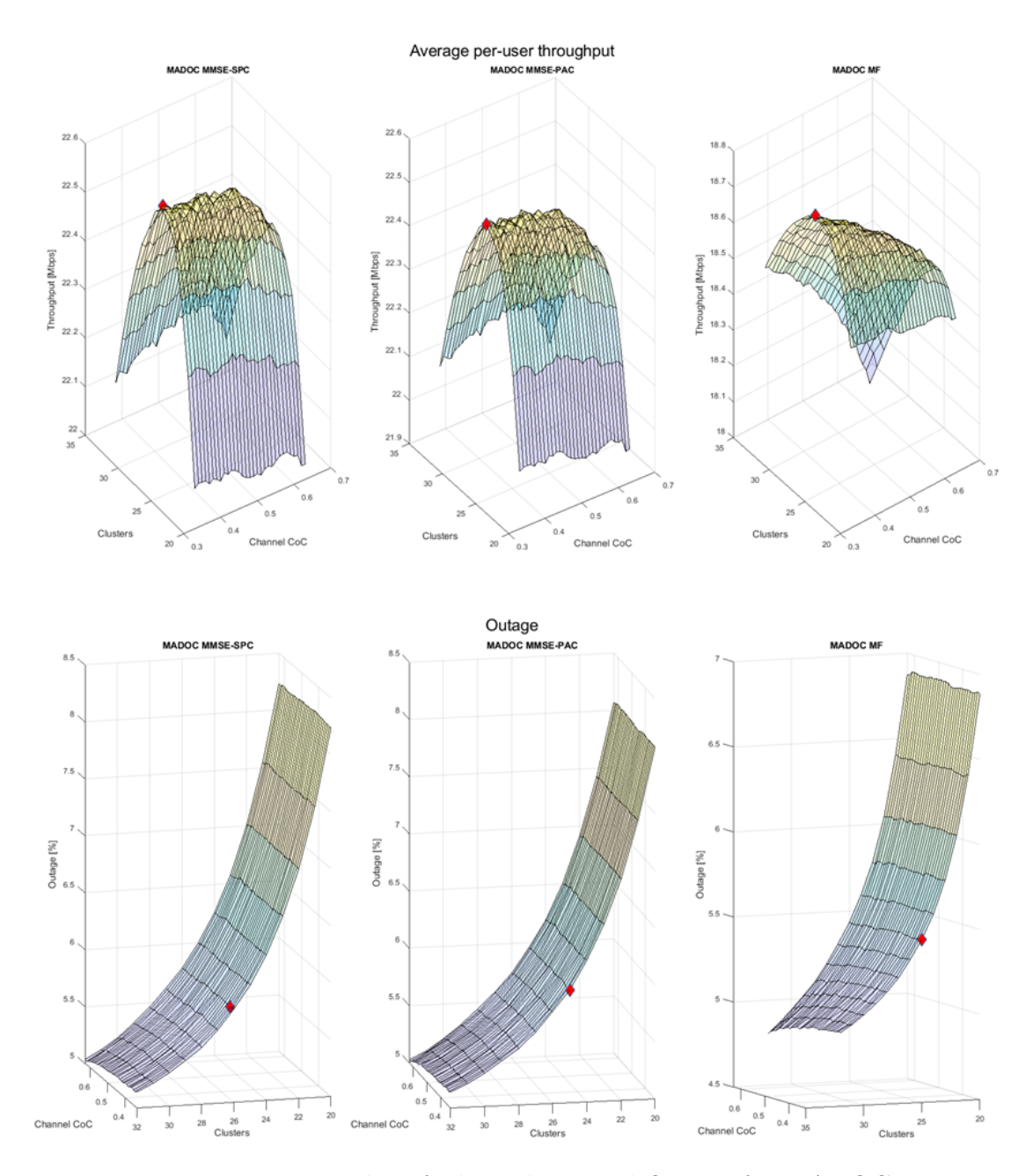


Figure 5.6: 3D Plot of Throughput and Outage for MADOC.

in Figure 5.10, where the MF-based H-RRM forms larger clusters compared to its LB-SLNR counterparts.

For the other algorithms (MADOC, D-MADOC, D-MCC-DSatur), the optimization similarly aims to maximize per-user throughput by selecting the optimal number of clusters. Table 5.6 summarizes the optimal values of the thresholds,

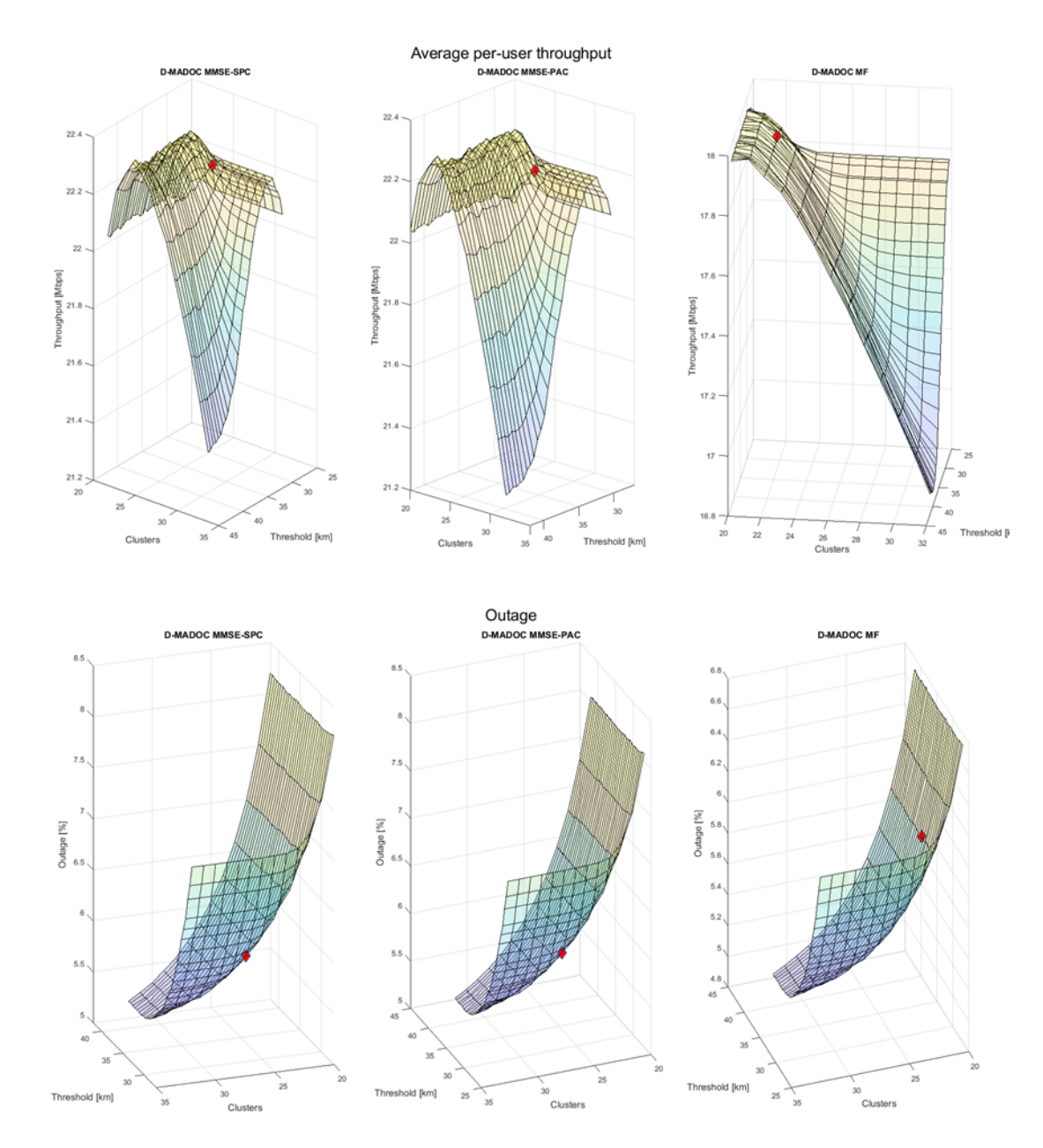


Figure 5.7: 3D Plot of Throughput and Outage for D-MADOC.

instead Table 5.7 summarizes the optimal number of clusters. The reduced value of EIRP forces the algorithms to form more clusters, which are smaller in size than before. This behavior is evident in the corresponding cluster size histograms of Figure 5.10 and has a direct impact on system performance, particularly in terms of sum-rate capacity and throughput. Compared to the previous EIRP configuration, where the median throughput was approximately 50 Mbps, the current results of

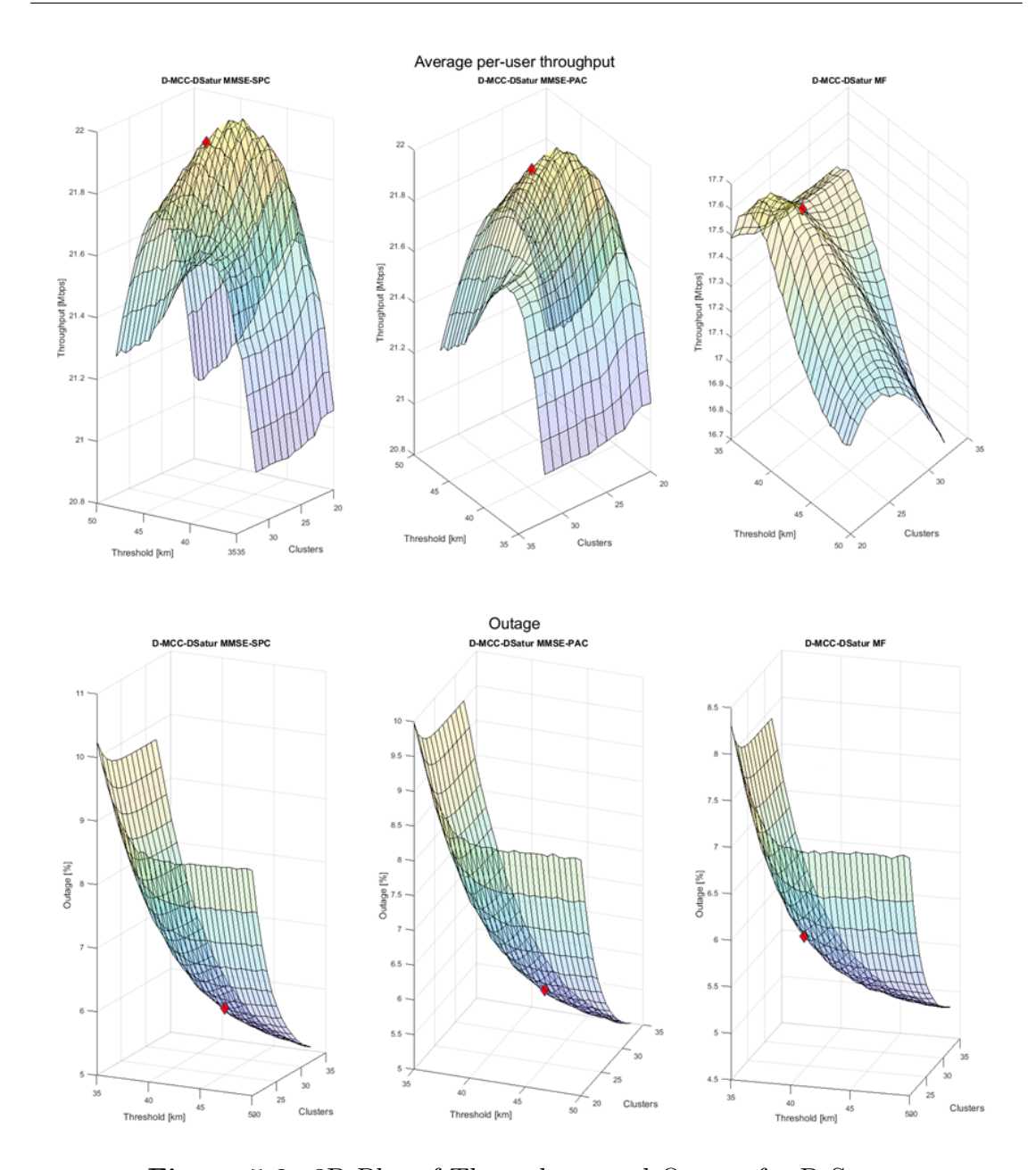


Figure 5.8: 3D Plot of Throughput and Outage for D-Satur.

Figure 5.12 show a reduction to around 15–20 Mbps, depending on the algorithm.

Similarly, in Figure 5.11, the sum-rate capacity is now observed at approximately 90-110 Gbps, highlighting the performance degradation caused by the lower transmit power and corresponding SINR loss. While D-MCC-DSatur previously achieved superior results, in this reduced power setting, its strategy of forming numerous small clusters appears to limit its efficiency. This is due to lower SINR and

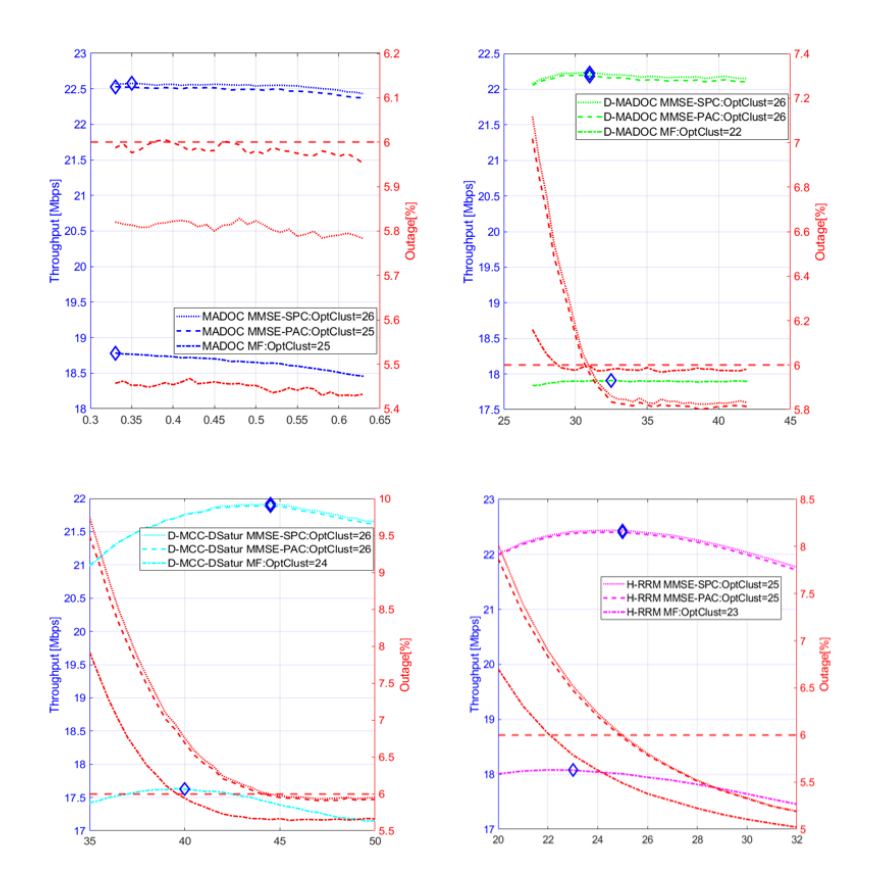


Figure 5.9: Optimal Threshold selection and corresponding outage.

weaker signal strength within these small clusters, leading to a drop in aggregate throughput.

D-MADOC, on the other hand achieves high peak sum-rate capacity, especially when combined with LB-SLNR beamforming, but it is affected by more dispersed cluster size distribution, leading to lower values of sum-rate for around 10% of the users. The effect of beamforming technique is also visible: LB-SLNR-based variants consistently outperform MF-based ones, due to their superior interference mitigation.

# 5.2 Performance Evaluation under Hybrid User Distribution

This chapter analyzes the system performance under a hybrid user distribution, where a fraction of users is uniformly distributed across the coverage area, while the remaining users are clustered around populated urban centers, as illustrated in

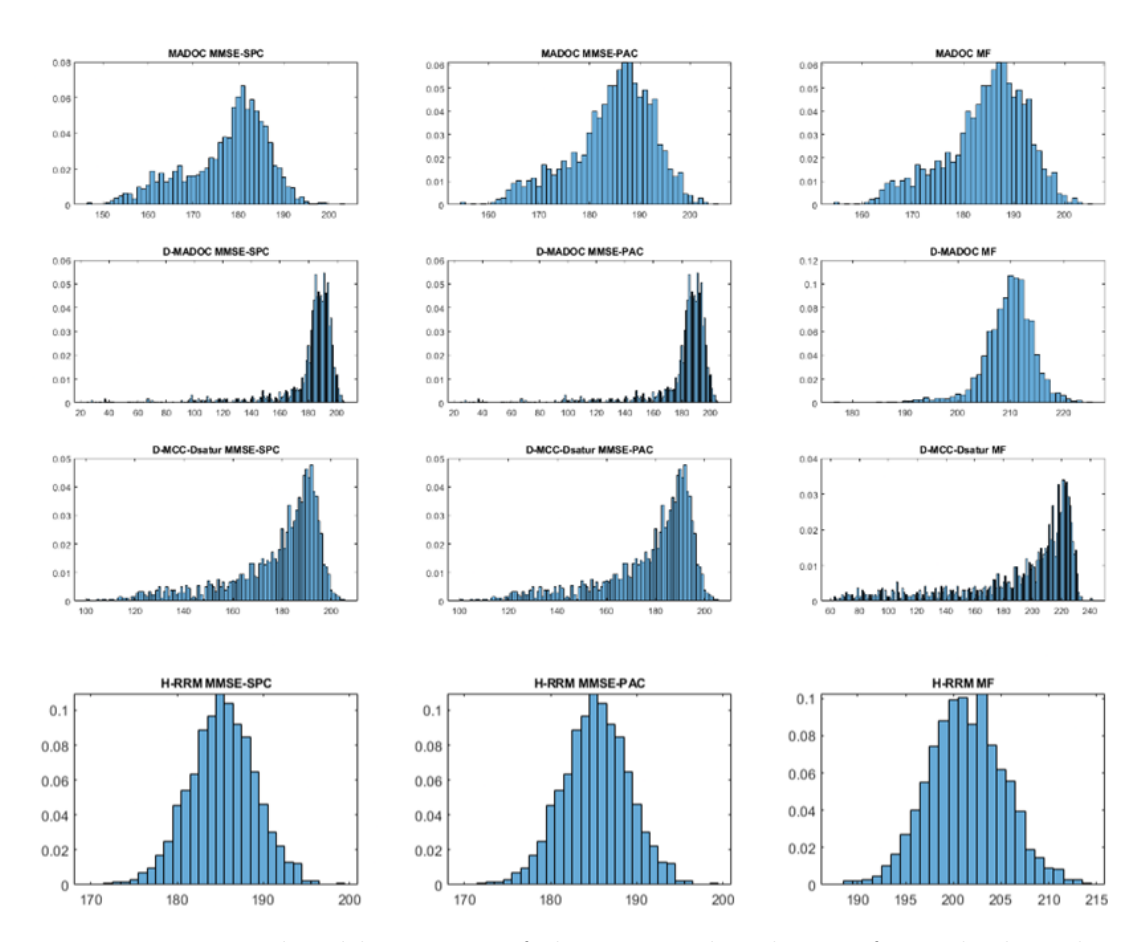


**Figure 5.10:** Updated histogram of cluster size distribution for each algorithm.

Fig. 3.6.

It is worth noting that, in this section, the performance evaluation is carried out exclusively for the H-RRM algorithm. This choice is motivated by its significantly lower computational complexity compared to the other scheduling schemes. As discussed in [10], H-RRM provides performance comparable to the Mixed Integer Quadratic Programming (MIQP)-based optimal solution, while exhibiting a computational complexity that scales approximately linearly with the number of users, rather than exponentially. This makes H-RRM particularly suitable for large-scale and heterogeneous user distributions, where the computational cost of the other algorithms would become prohibitive.

This part is organized as follows:

• Section 5.2.1 summarizes the results obtained when **all** users experience the same channel conditions corresponding to a sub-urban scenario as in the previous section 5.1.

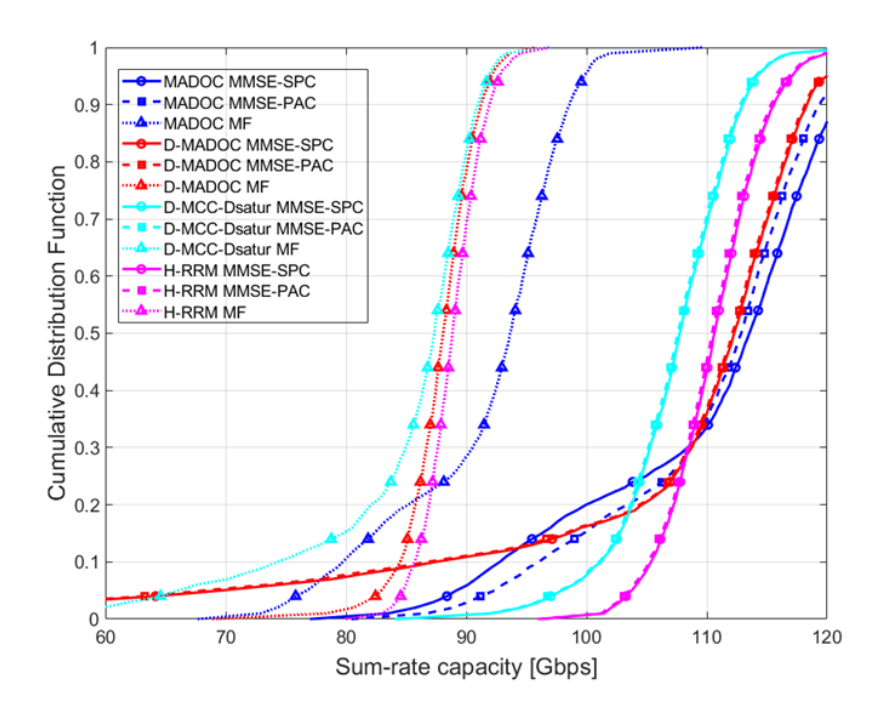


Figure 5.11: Updated Sum-Rate Capacity CDF Comparison Across Algorithms.

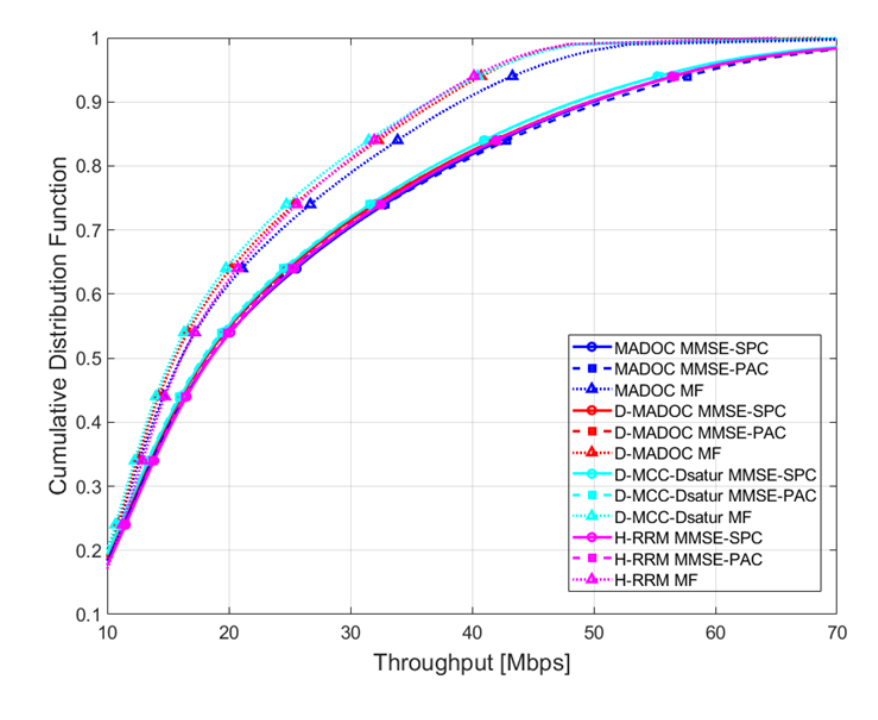


Figure 5.12: Updated Throughput CDF Comparison Across Algorithms.

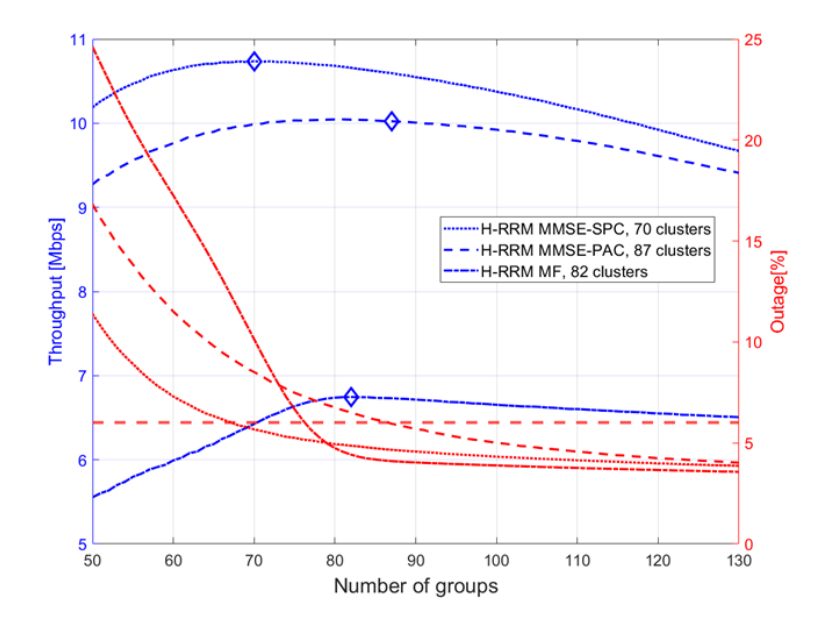


Figure 5.13: Optimal number of groups vs. Throughput and Outage

- Section 5.2.2 instead summarizes results obtained when **all** users experience dense urban channel conditions.
- Section 5.2.3 offers an overview on the performance of the scheduling and beamforming algorithms when each user experiences different channel conditions depending on the location. Users centered in cities experience dense-urban propagation conditions, whereas the others continue to experience sub-urban conditions.

#### 5.2.1 Sub-urban scenario

In this configuration, 80% of users are concentrated around urban centers and thus located in close proximity to one another. This increased user density presents a challenge for the clustering algorithm, as it must allocate resources more carefully to minimize interference. As a result, the number of clusters required increases significantly, reaching 70, 82, and 87, as shown in Figure 5.13. In line with these observations, the histograms shown in Figure 5.14 indicate a decrease in the number of users per cluster, with typical values ranging from 55 to 70 users per cluster, depending on the algorithm. Despite the denser spatial distribution, the system is still able to maintain the outage below the 6% threshold.

Figure 5.15 presents the CDF of the SINR. Overall, the SINR performance remains satisfactory, with less than 6% of users experiencing values below -6 dB.

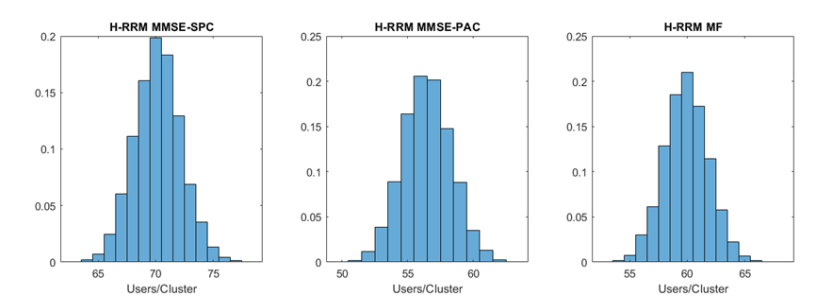


Figure 5.14: Histograms of users/cluster

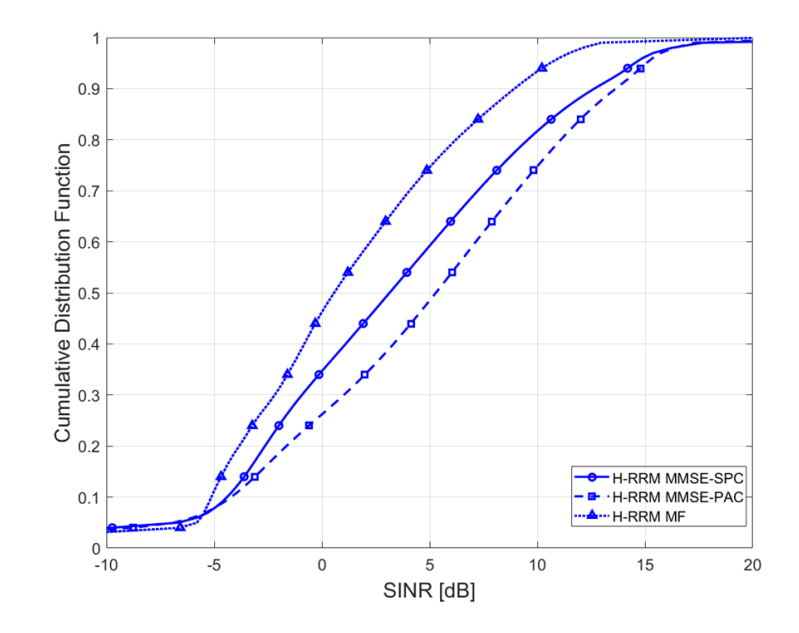


Figure 5.15: Cumulative Distribution Function of SINR

The median SINR is slightly reduced compared to previous scenarios, reaching up to 5 dB for H-RRM MMSE PAC, while the other algorithms achieve lower median values.

The sum-rate capacity shown in Figure 5.16 shows a reduction compared to the previous con-figuration. The median values are approximately 35 Gbps for H-RRM MF, 52 Gbps for H-RRM MMSE PAC, and 56 Gbps for H-RRM MMSE SPC. Figure 5.17 shows the CDF of the per-user throughput. Again, only a small percentile of users (approx-imately 6%) experience low achievable throughput. The median throughput is noticeably reduced, reaching around 5 Mbps for H-RRM MF, and approximately 10 Mbps for both H-RRM SPC and H-RRM MMSE PAC.

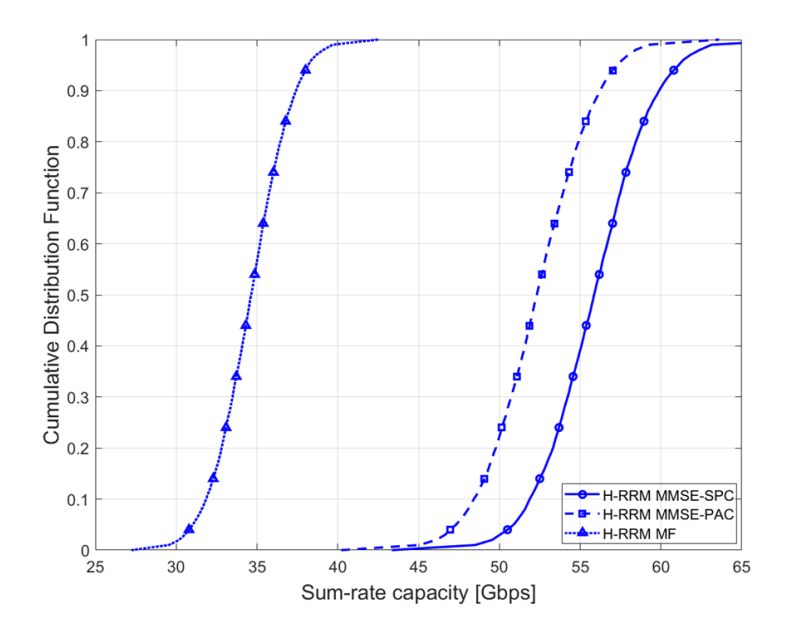


Figure 5.16: Cumulative Distribution Function of Sum-Rate Capacity

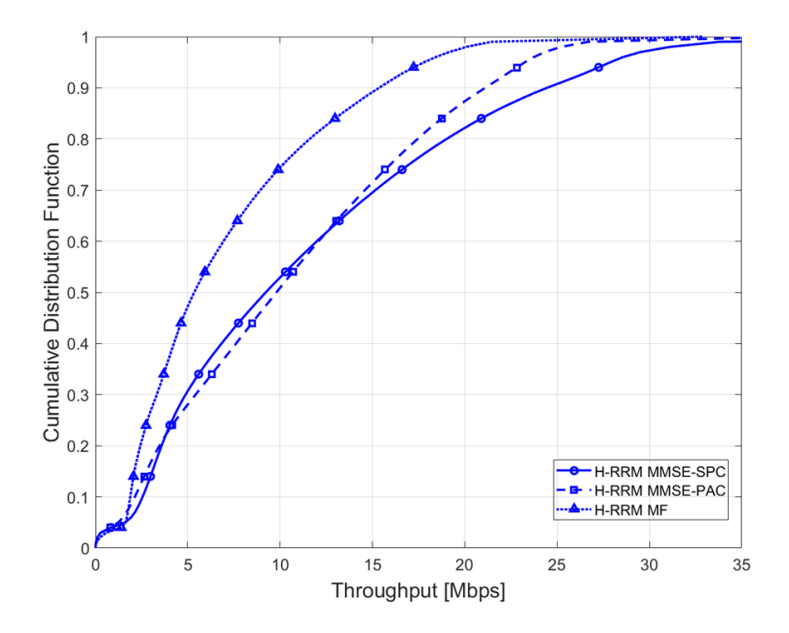


Figure 5.17: Cumulative Distribution Function of Throughput

#### 5.2.2 Dense urban scenario

In the dense urban scenario, the degradation in performance can be attributed primarily to changes in the large-scale propagation parameters, as defined by the 3GPP TR 38.811 channel model [37] summarized in Table 3.3. Compared to the sub-urban case of Table 3.4, the probability of Line-of-Sight (LOS) is significantly lower, especially at lower elevation angles, which increases the likelihood of Non-Line-of-Sight (NLOS) conditions. This, in turn, leads to higher shadow fading standard deviations and considerably greater clutter loss, with values reaching up to 44.3 dB compared to only 29.5 dB in sub-urban environments. These changes result in overall weaker received signal strength, reduced SINR, and lower throughput. While a decline in performance is expected, this section quantifies how much worse the system behaves under dense urban conditions by examining SINR distributions, throughput statistics, outage, and clustering behavior.

Figure 5.18 illustrates the relationship between the number of clusters, throughput, and outage. A key observation is the significant increase in outage, which reaches approximately 40%. Given the outage definition i.e., the percentage of users experiencing SINR below -6 dB, this indicates that 40% of users are operating under severely degraded signal conditions. To reach this level of outage, the number of clusters required rises to 86, 98 and 107 for the respective algorithms. From the corresponding histograms in Figure 5.19 it is evident that the number of users per cluster drops to between 40 and 55, which is noticeably lower than in previous scenarios, reflecting the higher spatial density and increased difficulty in separating users under dense urban conditions.

Figure 5.20 showing the CDF of the SINR provides insights into the SINR experienced by users, con-firming the findings from Figure 30. Specifically, it reveals that nearly 40% of users experienced an SINR below -6 dB, with the median SINR approximately at 0 dB. The SINR is directly affected by the EIRP which at this moment assumes a value of 20 dbW/MHz. The results indicate that on a link budget aspect, this value is not enough and therefore to increase the SINR a higher value of EIRP must be considered.

In terms of sum-rate capacity shown in Figure 5.21, the median values in the current dense urban scenario are significantly lower compared to the previous suburban scenario. Specifically, for H-RRM MF, the median sum-rate is around 23 Gbps, while for H-RRM MMSE SPC and PAC, it is approximately 35 Gbps. In the current scenario, the throughput for users considered in outage is quite low, with the median throughput around 2.5 Mbps for H-RRM MF and about 5 Mbps for H-RRM MMSE SPC and PAC, as shown in Figure 5.22.

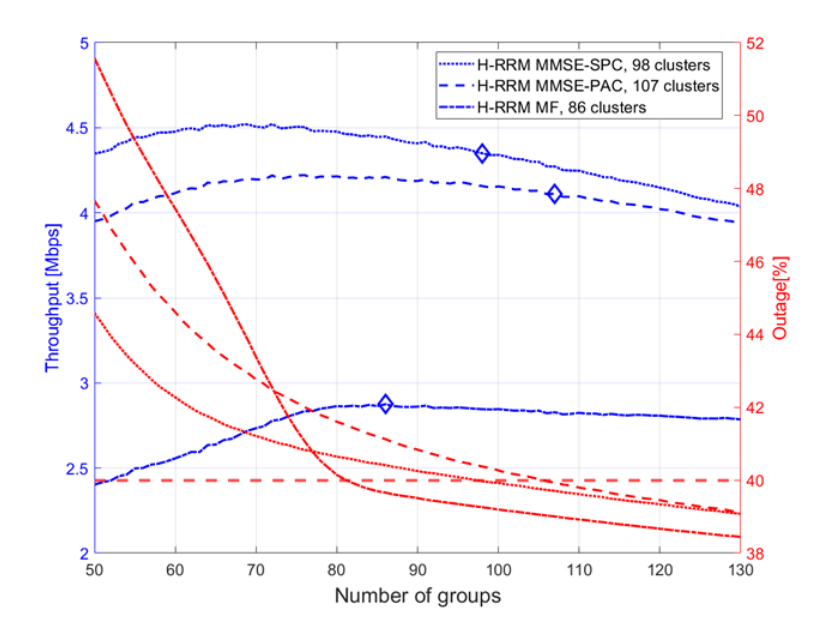


Figure 5.18: Optimal number of groups vs. Throughput and Outage

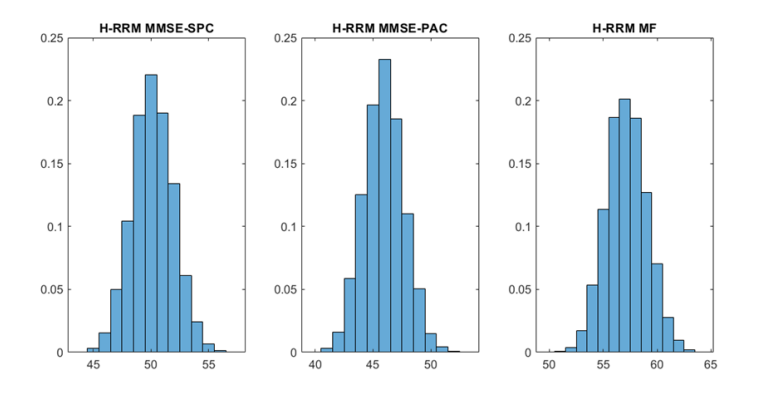


Figure 5.19: Histograms of users/cluster

#### 5.2.3 Adaptive scenario

In this section, we investigate how the EIRP value influences SINR, outage, and throughput, while considering an adaptive scenario on a per-user basis. Each user experiences different channel conditions depending on their spatial distribution: users clustered around cities are subjected to dense urban propagation conditions, while those uniformly distributed across the coverage area are modeled under suburban conditions. For the simulations we consider three different values of EIRP: 20, 30 and 40 dBW/MHz. A summary of the performance can be found in

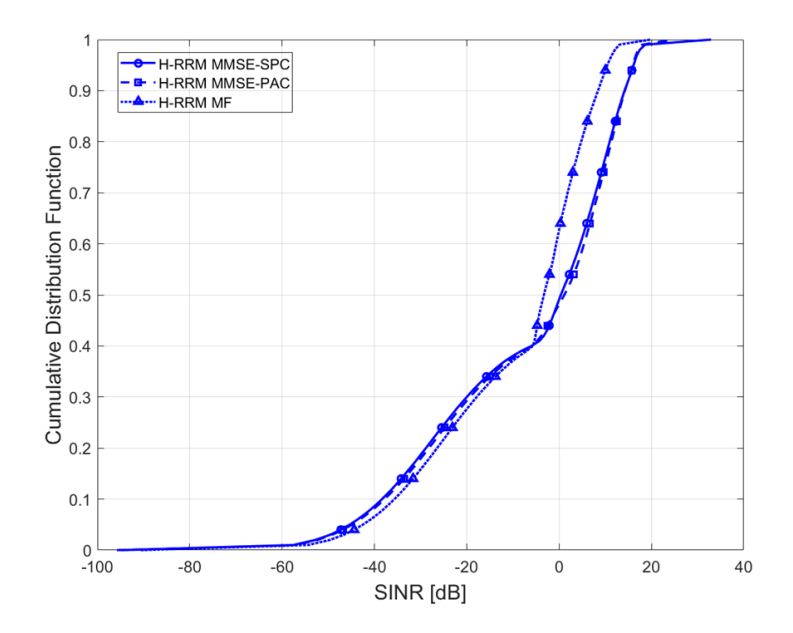


Figure 5.20: Cumulative Distribution Function of SINR

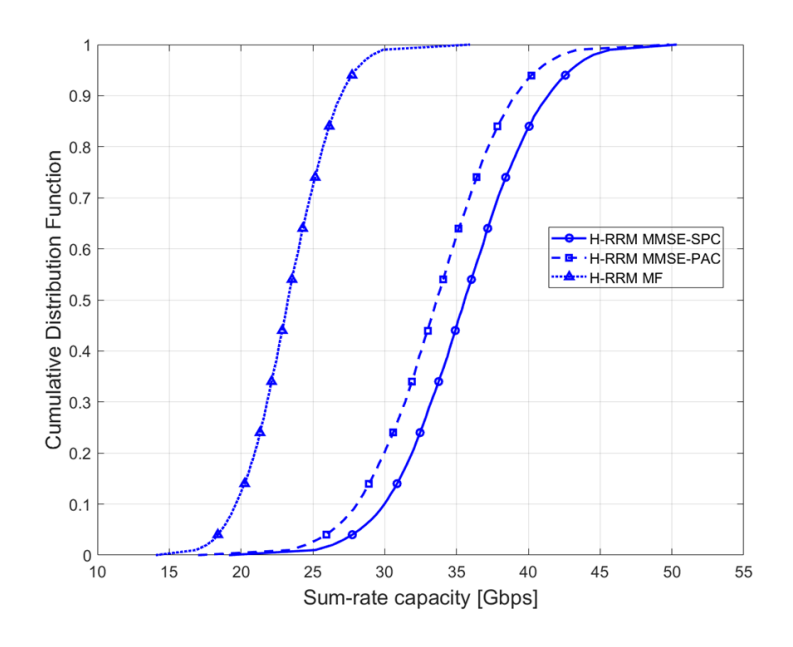


Figure 5.21: Cumulative Distribution Function of Sum-Rate Capacity

Table 5.8.

The optimal number of clusters is determined as before, by considering, as

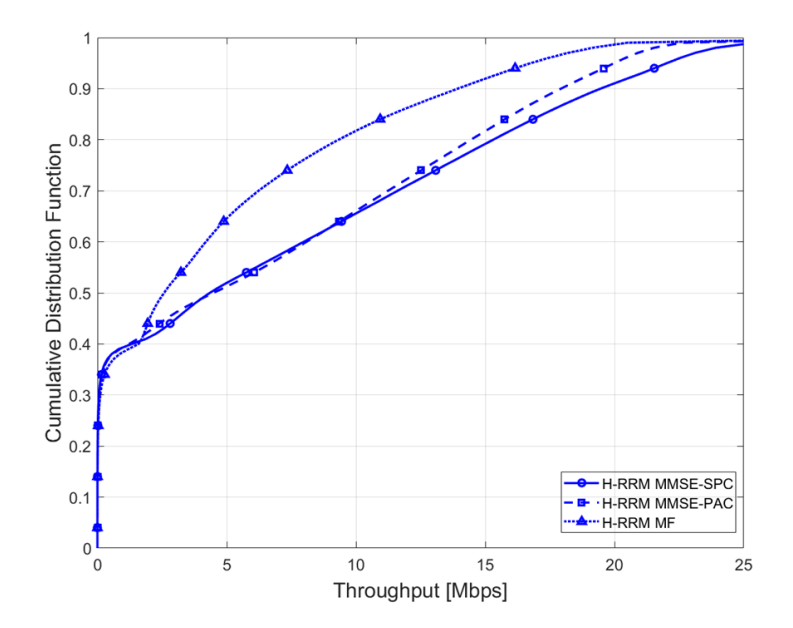


Figure 5.22: Cumulative Distribution Function of Throughput

**Table 5.8:** Summary of Adaptive Scenario Results for Different EIRP Values

EIRP [dBW/MHz]	Target Outage	Average Throughput [Mbps]		
		MF	$\mathbf{SPC}$	PAC
20	25%	5	~8	~8
30	18%	5	14	17
40	10%	6	36	23

before, the double optimization technique aiming to increase the per-user achievable throughput, while reducing the outage. The results of the simulations are shown in Figures 5.23, 5.24 and 5.25.

From the results presented in Figures 5.23–5.25 and summarized in Table 5.8, it can be observed that increasing the EIRP leads to a consistent improvement in the average throughput and a reduction in the outage probability across all beamforming strategies. At low EIRP values (20 dBW/MHz), all precoding schemes exhibit limited performance due to power constraints, resulting in comparable throughputs and higher outage levels. As the EIRP increases to 30 dBW/MHz, both SPC and PAC precoding schemes start to significantly outperform MF, indicating their better interference mitigation capability under higher transmit power. At 40 dBW/MHz, the system achieves its best performance, with the outage dropping to about 10% and a substantial increase in throughput, particularly for the SPC normalization variant, which reaches around 36 Mbps per user.

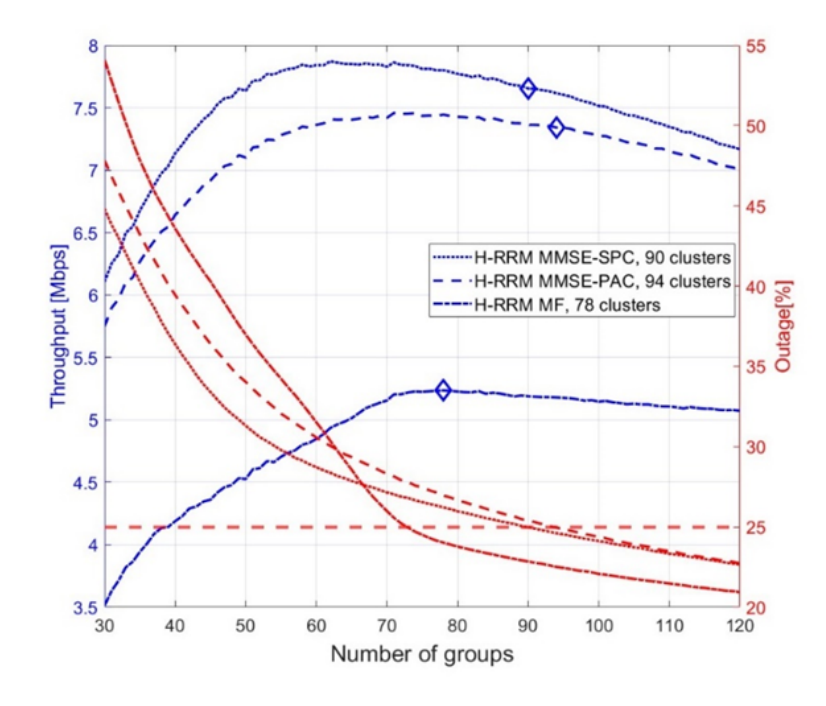


Figure 5.23: Adaptive Scenario: Threshold vs Throughput and Outage (EIRP=20  $\rm dbW/MHz)$ 

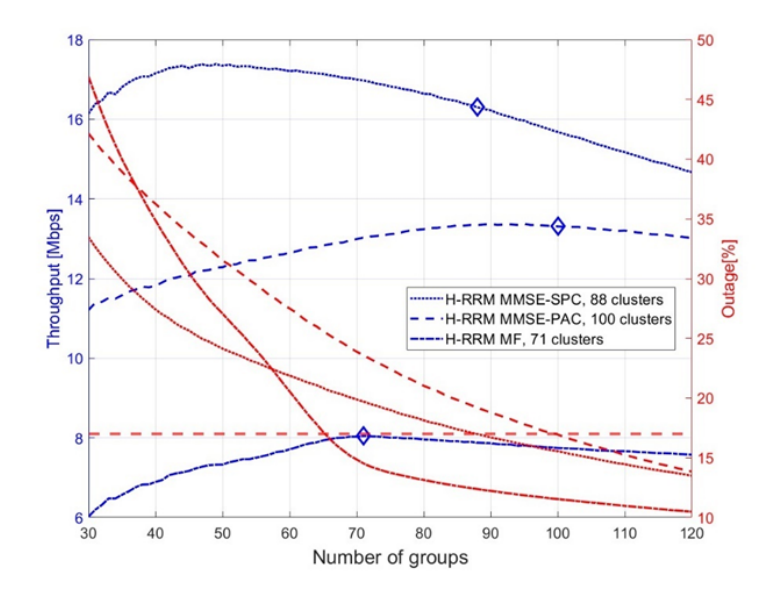


Figure 5.24: Adaptive Scenario: Threshold vs Throughput and Outage (EIRP=30  $\rm dbW/MHz)$ 

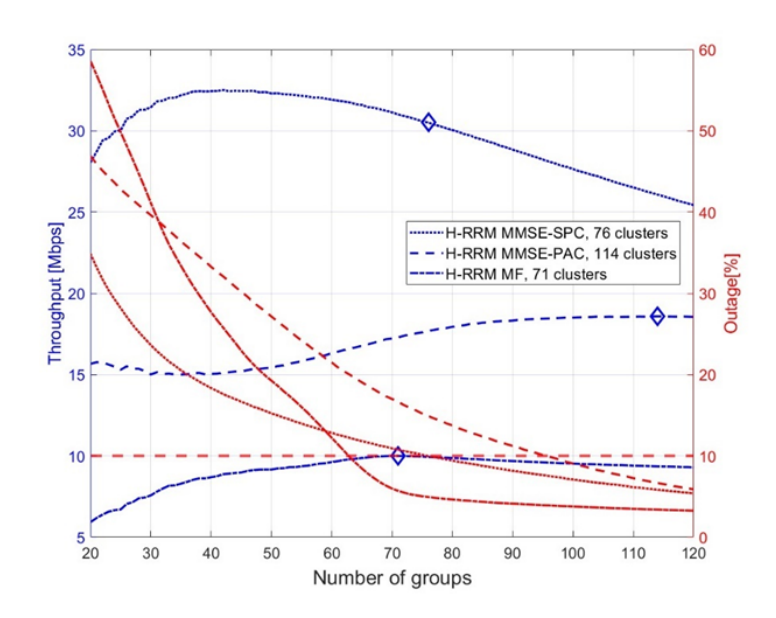


Figure 5.25: Adaptive Scenario: Threshold vs Throughput and Outage (EIRP=40  $\rm dbW/MHz)$ 

## Chapter 6

## Conclusion and Future Work

#### 6.1 Multi-Satellite Scenario

The rapid growth of Low Earth Orbit (LEO) constellations has caused a significant change in satellite communications. There is now more focus on multi-satellite cooperation to overcome the limits of traditional single-satellite systems. Earlier non-terrestrial network (NTN) designs mainly viewed satellites as separate units serving different user groups. However, new developments in distributed architectures and multi-user MIMO techniques are leading to coordinated multi-satellite systems. In these systems, several satellites work together as a distributed antenna array. This approach is especially important for Very Low Earth Orbit (VLEO) systems. The lower altitude of these satellites results in reduced latency and better link budgets, but it also requires more frequent handovers and more complex resource management.

Recent research has explored the evolution of cell-free and federated MIMO architectures for Non-Terrestrial Networks (NTNs) as a means to provide high-throughput, globally connected 6G systems. In [21], the authors introduced centralized and federated cell-free massive MIMO (CF-MIMO) architectures for NTNs, where multiple satellites cooperate as distributed access points within the same swarm to perform joint transmission. The study introduces a location-based CF-MIMO algorithm that operates without full channel state information and develops normalization techniques to handle non-colocated radiating elements, demonstrating strong performance even under imperfect conditions. Building on these concepts, [44] investigates federated beamforming with subarrayed planar antennas for distributed MIMO in multi-satellite swarms. By limiting the field of view and organizing antennas into smaller subarrays, the proposed design enhances beam directivity and interference mitigation, achieving higher spectral efficiency compared to conventional architectures.

In [45], the authors introduced the concept of distributed massive MIMO in LEO networks. They showed that coordinated transmission between multiple satellites can produce substantial spatial multiplexing gains, improve spectral efficiency, and enhance interference management. Authors in [46] underline the importance of architectural models and synchronization techniques for distributed satellite systems, focusing on different approaches such as clustered or federated constellations.

From an application perspective, in [47], authors evaluate the feasibility of distributed MIMO for broadband connectivity to handheld devices, demonstrating how multi-satellite cooperation can overcome the link budget limitations imposed by small, power-constrained devices. Their findings suggest that cooperative transmission is not only a theoretical construct but a practical solution for extending NTN broadband services to mobile users.

In [48], the authors provide a thorough evaluation of digital beamforming algorithms for multi-user MIMO in B5G/6G satellite systems. Their results highlight the importance of effective precoding and scheduling in maximizing throughput and fairness, while reducing interference. These insights are particularly relevant for VLEO systems, where the short orbital period and quick changes in user-satellite geometry require flexible, low-latency beamforming and resource allocation strategies.

The work on the multi-satellite scenario presented in this thesis should be regarded as an initial exploration. The current study has focused primarily on coverage and visibility aspects, establishing the conditions under which users may be simultaneously served by multiple satellites. Although preliminary, this analysis provides a foundation for future investigations into link-level performance, cooperative scheduling and beamforming strategies in Very Low Earth Orbit constellations.

The reference constellation considered in this work is shown in Figure 6.1 and contains 2118 satellites deployed in Very Low Earth Orbit (VLEO) at an altitude of approximately 300 km and an inclination of 54°.

The analysis has been narrowed down to 4 satellites, covering mainly Germany, as shown in Figure 6.2. The corresponding IDs of the satellites are shown in the picture.

In order to align better with the geometry of the satellites, the uniform user distribution considered previously has been slightly modified to form a rectangle shape as shown in Figure 6.3.

In order to manage the overlap of the satellites, a maximum off-nadir angle  $\eta_{max} = 45^{\circ}$  has been imposed. It is important to note that an elevation angle of  $\epsilon = 0^{\circ}$  is never considered as the coverage limit in satellite communication systems. At such low angles, foreshortening effects near the horizon distort the observed area, and obstacles such as terrain or buildings are more likely to obstruct

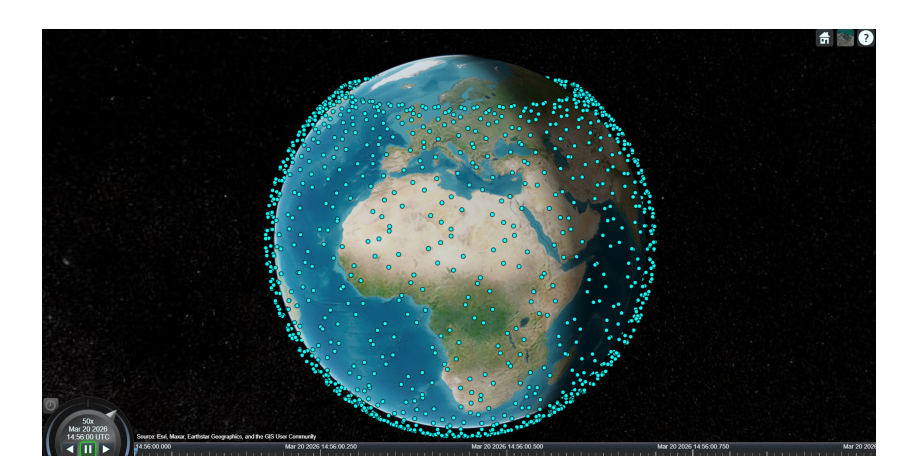


Figure 6.1: VLEO Constellation for Multi-Sat scenario.



Figure 6.2: Satellites considered for the coverage of Germany.

the line-of-sight, leading to non-line-of-sight (NLOS) propagation conditions. For this reason, a minimum elevation angle  $\epsilon_{\min}$  is typically defined as the coverage requirement to ensure reliable visibility and link quality. This constraint, however, reduces the satellite's effective field of view (FoV), as it limits the range of off-nadir angles that can be used to serve users on the ground. The relationship between the minimum elevation angle and the maximum nadir (or off-nadir) angle  $\eta_{\max}$  can be derived as:

$$\sin(\eta_{\text{max}}) = \frac{R_E}{R_E + h_{\text{sat}}} \cos(\epsilon_{\text{min}}),$$

which can be rearranged to compute the minimum elevation angle as:

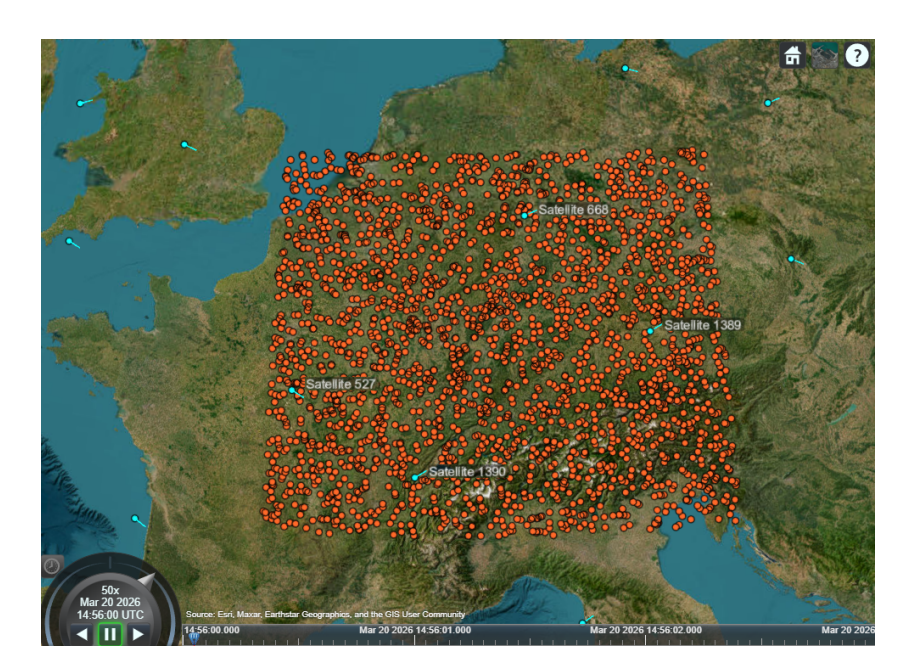


Figure 6.3: Rectangle uniform user distribution for Multi-Sat scenario.

$$\epsilon_{\min} = \arccos\left(\frac{R_E + h_{\text{sat}}}{R_E}\sin(\eta_{\text{max}})\right).$$

In this case, using this equation leads to the computation of the minimum elevation angle  $\epsilon_{min} = 42.258^{\circ}$ .

The off-nadir angle is used to determine whether a user lies within the coverage footprint of a given satellite, while the elevation angle criterion defines whether the satellite is considered visible to the user. User-satellite association is then performed by applying the elevation threshold: if the elevation angle is below  $\epsilon_{\min}$ , the satellite is excluded from the set of visible candidates. As expected in such a dense VLEO constellation, a significant fraction of users are simultaneously within the visibility region of multiple satellites, as illustrated in Figure 6.4. Some users in further areas cannot see any satellite, therefore they are excluded from the plot. Each user is color-coded according to the number of satellites it can simultaneously observe. As shown in Figure 6.4, users located near the center of the coverage region may have visibility of up to four satellites, while moving toward the edges of the footprint the number of visible satellites gradually decreases.

The analysis presented here offers a first step toward understanding multisatellite operation in Very Low Earth Orbit constellations. By defining a reference constellation, setting up a user distribution, and applying visibility criteria, the study has shown that users in dense VLEO systems are frequently covered by multiple satellites at the same time. This finding highlights both the opportunities

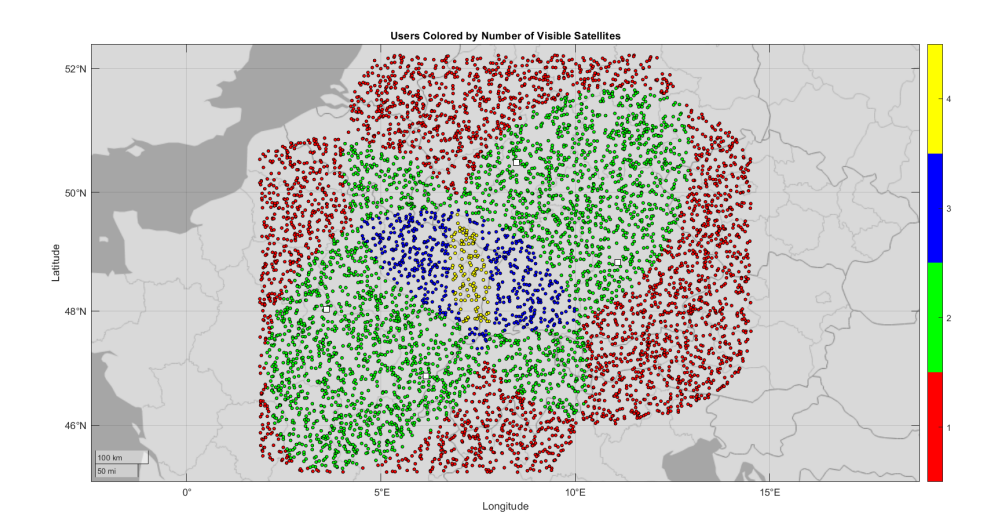


Figure 6.4: User distribution and the satellites visible to each user.

and the challenges of cooperative satellite operation. While the current work has focused mainly on coverage and visibility mapping, it lays the foundation for more detailed investigations.

A natural next step is to move beyond coverage and examine the actual communication performance. This includes studying the signal-to-interference-plus-noise ratio (SINR), achievable data rates, and the effect of different scheduling strategies when several satellites serve the same group of users. Another important aspect is the use of multi-user MIMO and coordinated beamforming. Evaluating different precoding techniques would help quantify the spatial multiplexing gains and interference reduction that could be achieved through cooperation between satellites.

Because VLEO satellites move rapidly across the sky, frequent handovers are unavoidable. Designing and testing efficient handover strategies will therefore be essential to ensure service continuity for mobile users. A further extension of the work would be to introduce realistic traffic models and non-uniform user distributions, making the analysis more representative of real deployment scenarios. Combining these with resource allocation policies at different system layers would provide a clearer picture of the trade-offs in performance, efficiency, and complexity.

In summary, the present study provides an initial look at coverage in a multi-satellite VLEO system. Future work will expand this perspective by integrating link-level performance, scheduling, beamforming, and handover management, aiming to maximize the true potential of distributed multi-satellite architectures for next-generation non-terrestrial networks.

### 6.2 Conclusion

The joint challenges of beamforming and user scheduling in multi-user MIMO settings were the main focus of this thesis' investigation of advanced Radio Resource Management (RRM) techniques for Very Low Earth Orbit (VLEO) Non-Terrestrial Networks (NTNs). In order to evaluate the trade-offs between spectral efficiency, user fairness, and robustness in dynamic satellite-terrestrial environments, the work was conducted as part of the European Space Agency's HANDING-OVER project.

This thesis primarily contributed to the assessment and modification of advanced scheduling algorithms, such as, MADOC, D-MADOC, D-MCC-DSatur, and Heuristic-RRM, alongside their benchmarking against various beamforming techniques, specifically location-based MMSE (LB-SLNR) and matched filtering (beam-steering). The analysis covered various scenarios, including uniform user distributions, dense-urban environments, and hybrid deployments, while incorporating variations in satellite transmit power by changing the value of the Equivalent Isotropically Radiated Power (EIRP). Several conclusions can be derived from the results.

• Uniform user distribution:

With optimal propagation conditions and higher EIRP (30 dBW/MHz), all algorithms demonstrated good performance, delivering per-user throughput around 50 Mbps and sum-rate capacities larger than 200 Gbps.

MADOC and D-MADOC attained the highest peak sum rates, nearing 290 Gbps; however, their performance presented inconsistency among users due to the appearance of small, uneven clusters.

H-RRM and D-MCC-DSatur display more stable throughput distributions and narrower cluster size variations, resulting in a fairer resource allocation and greater robustness within the user population.

Scenario of reduced Effective Isotropic Radiated Power (20 dBW/MHz):
 A further drop in performance was observed with median throughput decreasing to 15–20 Mbps and total capacity to 90–110 Gbps.

The outage emerged as a crucial metric: although MADOC and D-MADOC attained peak rates, their failure to regulate the proportion of users beneath the SINR threshold constrained their practical utility.

H-RRM was consistently able to satisfy the outage constraint (<6%), demonstrating its ability to adapt in power-limited NTN conditions.

• With more users concentrated around cities, the distance between users becomes smaller, spatial correlation between UEs increased significantly, challenging both clustering and beamforming. In suburban scenarios, throughput

medians fell to 5-10 Mbps, while outages remained within acceptable limits (6%).

- In densely populated urban environments, however, outages grew significantly, affecting 40% of users, with low median SINR and throughput reduced to 2–5 Mbps. This clearly illustrates the constraints of existing scheduling and beamforming techniques in practical implementations, unless enhanced by greater EIRP or advanced interference mitigation strategies.
- Regarding the comparison of beamforming techniques, in all scenarios, LB-SLNR (location-based MMSE) beamforming consistently exceeded conventional beam-steering. The improvement was especially evident in interference-limited scenarios, where LB-SLNR achieved superior SINR distributions and an improved throughput allocation, proving the need for sophisticated precoding.
- Future analysis of the multi-satellite scenario should go beyond coverage and visibility to include link-level performance metrics. This would involve studying achievable throughput, outage probability, and interference management under different power budgets and user distributions. In particular, evaluating scheduling and beamforming techniques would provide insights into system fairness, robustness in dense-urban conditions, and the role of advanced precoding in realizing the potential of cooperative multi-satellite architectures.

# Bibliography

- [1] A. Vanelli-Coralli, A. Guidotti, T. Foggi, G. Colavolpe, and G. Montorsi. «5G and Beyond 5G Non-Terrestrial Networks: trends and research challenges». In: *Proc. IEEE 3rd 5G World Forum (5GWF)*. Bangalore, India, 2020, pp. 163–169 (cit. on p. 1).
- [2] S. Kota and G. Giambene. «6G Integrated Non-Terrestrial Networks: Emerging Technologies and Challenges». In: *Proc. IEEE International Conference on Communications Workshops (ICC Workshops)*. Montreal, QC, Canada, 2021, pp. 1–6 (cit. on p. 1).
- [3] M. R. Dakkak, D. G. Riviello, A. Guidotti, and A. Vanelli-Coralli. «Evaluation of multi-user multiple-input multiple-output digital beamforming algorithms in B5G/6G low Earth orbit satellite systems». In: *International Journal of Satellite Communications and Networking* (2023), pp. 1–17 (cit. on p. 1).
- [4] L. You, K.-X. Li, J. Wang, X. Gao, X.-G. Xia, and B. Ottersten. «Massive MIMO transmission for LEO satellite communications». In: *IEEE Journal on Selected Areas in Communications* 38.8 (2020), pp. 1851–1865 (cit. on p. 1).
- [5] E. Castañeda, A. Silva, A. Gameiro, and M. Kountouris. «An Overview on Resource Allocation Techniques for Multi-User MIMO Systems». In: *IEEE Communications Surveys & Tutorials* 19.1 (2017). First Quarter, pp. 239–284 (cit. on p. 1).
- [6] X. Yi and E. K. S. Au. «User Scheduling for Heterogeneous Multiuser MIMO Systems: A Subspace Viewpoint». In: *IEEE Transactions on Vehicular Tech*nology 60.8 (Oct. 2011), pp. 4004–4013 (cit. on p. 2).
- [7] K.-U. Storek and A. Knopp. «Fair User Grouping for Multibeam Satellites with MU-MIMO Precoding». In: *Proc. IEEE Global Communications Conference (GLOBECOM)*. Singapore: IEEE, 2017, pp. 1–7 (cit. on pp. 2, 28).
- [8] B. Ahmad, D. G. Riviello, B. De Filippo, A. Guidotti, and A. Vanelli-Coralli. «Analysis of Graph-based User Scheduling for Ka-band LEO NTN Systems». In: *Proc. 28th Ka and Broadband Communications Conference (Ka) and*

- 40th International Communications Satellite Systems Conference (ICSSC). Bradford, United Kingdom, 2023 (cit. on pp. 2, 28).
- [9] P. Angeletti and R. De Gaudenzi. «A Pragmatic Approach to Massive MIMO for Broadband Communication Satellites». In: *IEEE Access* 8 (2020), pp. 132212–132236 (cit. on p. 2).
- [10] P. Angeletti and R. De Gaudenzi. «Heuristic Radio Resource Management for Massive MIMO in Satellite Broadband Communication Networks». In: *IEEE Access* 9 (2021), pp. 147164–147199 (cit. on pp. 2, 49).
- [11] O. Kodheli et al. «Satellite Communications in the New Space Era: A Survey and Future Challenges». In: *IEEE Communications Surveys & Tutorials* 23.1 (2021), pp. 70–109. DOI: 10.1109/COMST.2020.3028247 (cit. on pp. 5, 9).
- [12] I. S. Mohamad Hashim and A. Al-Hourani. «Satellite-Based Localization of IoT Devices Using Joint Doppler and Angle-of-Arrival Estimation». In: Remote Sensing 15.23 (2023). Available: https://www.mdpi.com/2072-4292/15/23/5603, p. 5603. DOI: 10.3390/rs15235603 (cit. on p. 6).
- [13] F. Rinaldi, H.-L. Maattanen, J. Torsner, S. Pizzi, S. Andreev, A. Iera, Y. Koucheryavy, and G. Araniti. «Non-Terrestrial Networks in 5G and Beyond: A Survey». In: *IEEE Access* 8 (2020), pp. 165178–165200. DOI: 10.1109/ACCESS.2020.3015259 (cit. on p. 5).
- [14] C. Carballo González, S. Pizzi, M. Murroni, and G. Araniti. «Multicasting Over 6G Non-Terrestrial Networks: A Softwarization-Based Approach». In: *IEEE Vehicular Technology Magazine* 18.1 (2023), pp. 91–99. DOI: 10.1109/MVT.2022.3226759 (cit. on p. 5).
- [15] B. Li, Z. Fei, and Y. Zhang. «UAV Communications for 5G and Beyond: Recent Advances and Future Trends». In: *IEEE Internet of Things Journal* 6.2 (2019), pp. 2241–2263. DOI: 10.1109/JIOT.2018.2887086 (cit. on p. 7).
- [16] M. Marchese, A. Moheddine, and F. Patrone. «IoT and UAV Integration in 5G Hybrid Terrestrial-Satellite Networks». In: Sensors 19.17 (2019), p. 3704. DOI: 10.3390/s19173704 (cit. on p. 7).
- [17] L. Reynaud and T. Rasheed. «Deployable Aerial Communication Networks: Challenges for Futuristic Applications». In: *Proceedings of the 9th ACM Symposium on Performance Evaluation of Wireless Ad Hoc, Sensor, and Ubiquitous Networks.* 2012, pp. 1–4. DOI: 10.1145/2387191.2387193 (cit. on p. 7).
- [18] M. Conti. «Satellite Systems in the Era of 5G Internet of Things». Available: https://amsdottorato.unibo.it/id/eprint/9879/. PhD thesis. Bologna, Italy: Department of Electrical, Electronic and Information Engineering, University of Bologna, 2020 (cit. on p. 8).

- [19] G. Maral, M. Bousquet, and Z. Sun. Satellite Communications Systems: Systems, Techniques and Technology. 6th. Wiley, 2020. ISBN: 9781119383090 (cit. on p. 8).
- [20] Z. Dong, L. Yi, P. Qin, Y. Zhou, C. Zhang, and K. Liu. «Quantification and Analysis of Carrier-to-Interference Ratio in High-Throughput Satellite Systems». In: *Electronics* 12.16 (2023), p. 3504. DOI: 10.3390/electronics 12163504 (cit. on pp. 8, 9).
- [21] A. Guidotti, A. Vanelli-Coralli, and C. Amatetti. «Federated Cell-Free MIMO in Non-Terrestrial Networks: Architectures and Performance». In: arXiv preprint (2023). arXiv:2302.00057 (cit. on pp. 8, 60).
- [22] 3GPP. Global Standardization (Official Website). https://www.3gpp.org/about-us. Accessed: 2025-10-03 (cit. on p. 10).
- [23] 3GPP. Technical Specification Group Radio Access Network; Study on New Radio (NR) to Support Non Terrestrial Networks. Tech. rep. TR 38.811 V15.2.0. 3rd Generation Partnership Project (3GPP), Sept. 2019 (cit. on p. 10).
- [24] 3GPP. Technical Specification Group Radio Access Network; Solutions for NR to Support Non-Terrestrial Networks. Tech. rep. TR 38.821 V0.9.0. 3rd Generation Partnership Project (3GPP), Sept. 2019 (cit. on p. 10).
- [25] 3GPP. 5G in Release 17 Strong Radio Evolution. Tech. rep. TR 38.821 V0.9.0. 3rd Generation Partnership Project (3GPP), Jan. 2020 (cit. on p. 11).
- [26] 3GPP. Technical Specification Group Services and System Aspects; Study on Using Satellite Access in 5G. Tech. rep. TR 38.822 V16.0.0. Sophia Antipolis, France: 3rd Generation Partnership Project (3GPP), June 2018 (cit. on p. 11).
- [27] X. Fang, W. Feng, T. Wei, Y. Chen, N. Ge, and C.-X. Wang. «5G Embraces Satellites for 6G Ubiquitous IoT: Basic Models for Integrated Satellite Terrestrial Networks». In: *IEEE Internet of Things Journal* 8.18 (2021), pp. 14399–14417. DOI: 10.1109/JIOT.2021.3079487 (cit. on p. 11).
- [28] X. Zhu and C. Jiang. «Integrated Satellite-Terrestrial Networks Toward 6G: Architectures, Applications, and Challenges». In: *IEEE Internet of Things Journal* 9.1 (2022), pp. 437–461. DOI: 10.1109/JIOT.2021.3082045 (cit. on p. 11).
- [29] X. Lin, S. Cioni, G. Charbit, N. Chuberre, S. Hellsten, and J.-F. Boutillon. «On the Path to 6G: Embracing the Next Wave of Low Earth Orbit Satellite Access». In: *IEEE Communications Magazine* 59.12 (2021), pp. 36–42. DOI: 10.1109/MCOM.001.2100495 (cit. on p. 11).

- [30] H. Xie, Y. Zhan, G. Zeng, and X. Pan. «LEO Mega Constellations for 6G Global Coverage: Challenges and Opportunities». In: *IEEE Access* 9 (2021), pp. 164223–164244. DOI: 10.1109/ACCESS.2021.3135071 (cit. on p. 11).
- [31] A. Guidotti, A. Vanelli-Coralli, V. Schena, N. Chuberre, M. El Jaafari, J. Puttonen, and S. Cioni. «The Path to 5G-Advanced and 6G Non-Terrestrial Network Systems». In: 2022 11th Advanced Satellite Multimedia Systems Conference and the 17th Signal Processing for Space Communications Workshop (ASMS/SPSC). 2022, pp. 1–8. DOI: 10.1109/ASMS/SPSC55218.2022. 9840187 (cit. on p. 11).
- [32] Solutions for NR to support Non-Terrestrial Networks (NTN) (Release 16). 3rd Generation Partnership Project (3GPP), Mar. 2023 (cit. on p. 12).
- [33] 3GPP. Study on channel model for frequencies from 0.5 to 100 GHz (Release 16). Technical Report TR 38.901. 3rd Generation Partnership Project (3GPP), Nov. 2020 (cit. on p. 14).
- [34] ITU-R Radiocommunication Sector. Modelling and simulation of IMT networks and systems for use in sharing and compatibility studies. Feb. 2017 (cit. on p. 14).
- [35] D. G. Riviello, R. Tuninato, and R. Garello. «Multi-Layer Multi-User MIMO With Cylindrical Arrays Under 3GPP 3D Channel Model for B5G/6G Networks». In: *IEEE Access* 12 (2024), pp. 145753–145767. DOI: 10.1109/ACCESS. 2024.3391163 (cit. on p. 14).
- [36] G. Alfano, C.-F. Chiasserini, A. Nordio, and D. G. Riviello. «A Random Matrix Model for mmWave MIMO Systems». In: *Acta Physica Polonica B* 51.7 (2020), pp. 1627–1640 (cit. on p. 14).
- [37] 3GPP. TR 38.811 Study on New Radio (NR) to support non-terrestrial networks (Release 15). Technical Report TR 38.811. 3rd Generation Partnership Project (3GPP), Oct. 2020 (cit. on pp. 15–18, 54).
- [38] D. G. Riviello, B. De Filippo, B. Ahmad, A. Guidotti, and A. Vanelli-Coralli. «Location-based User Scheduling through Graph Coloring for Cell-Free MIMO NTN Systems». In: *Proc. 2024 Joint European Conference on Networks and Communications & 6G Summit (EuCNC/6G Summit)*. Antwerp, Belgium: IEEE, 2024, pp. 652–657 (cit. on pp. 15, 31).
- [39] ITU-R. Recommendation ITU-R P.676-13: Attenuation by atmospheric gases. Tech. rep. Geneva, Switzerland. International Telecommunication Union, Radiocommunication Sector (ITU-R), 2023 (cit. on p. 17).

- [40] ITU-R. Recommendation ITU-R P.618-14: Propagation data and prediction methods required for the design of Earth-space telecommunication systems. Tech. rep. Geneva, Switzerland. International Telecommunication Union, Radiocommunication Sector (ITU-R), 2023 (cit. on p. 18).
- [41] Wikimedia Commons contributors. 3D Spherical Coordinate System. https://en.wikipedia.org/wiki/File:3D\_Spherical.svg. Licensed under CC BY-SA 3.0. 2006 (cit. on p. 20).
- [42] Wikipedia contributors. Rotation matrix Wikipedia, The Free Encyclopedia. 2025. URL: https://en.wikipedia.org/wiki/Rotation\_matrix (cit. on p. 21).
- [43] D. Brélaz. «New methods to color the vertices of a graph». In: Communications of the ACM 22.4 (1979), pp. 251–256 (cit. on p. 31).
- [44] M. Rabih Dakkak, Daniel Gaetano Riviello, Alessandro Guidotti, and Alessandro Vanelli–Coralli. «Federated Beamforming with Subarrayed Planar Arrays for B5G/6G LEO Non-Terrestrial Networks». In: 2024 IEEE Wireless Communications and Networking Conference (WCNC). 2024, pp. 01–06. DOI: 10.1109/WCNC57260.2024.10571202 (cit. on p. 60).
- [45] Mohammed Y. Abdelsadek, Gunes Karabulut Kurt, and Halim Yanikomeroglu. «Distributed Massive MIMO for LEO Satellite Networks». In: *IEEE Open Journal of the Communications Society* 3 (2022), pp. 2162–2177. DOI: 10.1109/0JC0MS.2022.3219419 (cit. on p. 61).
- [46] Liz Martinez Marrero, Juan Carlos Merlano-Duncan, Jorge Querol, Sumit Kumar, Jevgenij Krivochiza, Shree Krishna Sharma, Symeon Chatzinotas, Adriano Camps, and Björn Ottersten. «Architectures and Synchronization Techniques for Distributed Satellite Systems: A Survey». In: *IEEE Access* 10 (2022), pp. 45375–45409. DOI: 10.1109/ACCESS.2022.3169499 (cit. on p. 61).
- [47] Mohammed Y. Abdelsadek, Gunes Karabulut-Kurt, Halim Yanikomeroglu, Peng Hu, Guillaume Lamontagne, and Khaled Ahmed. «Broadband Connectivity for Handheld Devices via LEO Satellites: Is Distributed Massive MIMO the Answer?» In: *IEEE Open Journal of the Communications Society* 4 (2023), pp. 713–726. DOI: 10.1109/0JC0MS.2023.3253643 (cit. on p. 61).
- [48] Xuan Zhang, Shu Sun, Meixia Tao, Qin Huang, and Xiaohu Tang. «Multi-Satellite Cooperative Networks: Joint Hybrid Beamforming and User Scheduling Design». In: *IEEE Transactions on Wireless Communications* 23.7 (2024), pp. 7938–7952. DOI: 10.1109/TWC.2023.3346463 (cit. on p. 61).